ACSNANO

www.acsnano.org

ARTICLE

Tuning Ligand Density To Optimize Pharmacokinetics of Targeted Nanoparticles for Dual Protection against Tumor-Induced Bone Destruction

Joseph Vanderburgh, Jordan L. Hill, Mukesh K. Gupta, Kristin A. Kwakwa, Sean K. Wang, Kathleen Moyer, Sean K. Bedingfield, Alyssa R. Merkel, Richard d'Arcy, Scott A. Guelcher, Julie A. Rhoades, and Craig L. Duvall*

Cite This: *ACS Nano* 2020, 14, 311–327

Read Online

ACCESS | Metrics & More | Article Recommendations | Supporting Information

ABSTRACT: Breast cancer patients are at high risk for bone metastasis. Metastatic bone disease is a major clinical problem that leads to a reduction in mobility, increased risk of pathologic fracture, severe bone pain, and other skeletal-related events. The transcription factor Gli2 drives expression of parathyroid hormone-related protein (PTHrP), which activates osteoclast-mediated bone destruction, and previous studies showed that Gli2 genetic repression in bone-metastatic tumor cells significantly reduces tumor-induced bone destruction. Small molecule inhibitors of Gli2 have been identified; however, the lipophilicity and poor pharmacokinetic profile of these compounds have precluded their success *in vivo*. In this study, we designed a bone-targeted nanoparticle (BTNP) comprising an amphiphilic diblock copolymer of poly-[(propylene sulfide)-*block*-(alendronate acrylamide-*co*-*N*,*N*-dimethylacrylamide)] [PPS-*b*-P(Aln-*co*-DMA)] to encapsulate and preferentially deliver a small molecule Gli2 inhibitor, GANT58, to bone-associated tumors. The mol % of the bisphosphonate Aln in the hydrophilic polymer block was varied in order to optimize BTNP targeting to tumor-associated bone by a combination of nonspecific tumor accumulation (presumably through the enhanced permeation and retention effect) and active bone binding. Although 100% functionalization with Aln created BTNPs with strong bone binding, these BTNPs had highly negative zeta-potential, resulting in shorter circulation time, greater liver uptake, and less distribution to metastatic tumors in bone. However, 10 mol % of Aln in the hydrophilic block generated a formulation with a favorable balance of systemic pharmacokinetics and bone binding, providing the highest bone/liver biodistribution ratio among formulations tested. In an intracardiac tumor cell injection model of breast cancer bone metastasis, treatment with the lead candidate GANT58-BTNP formulation decreased tumor-associated bone lesion area 3-fold and increased bone volume fraction in the tibiae of the mice 2.5-fold. Aln conferred bone targeting to the GANT58-BTNPs, which increased GANT58 concentration in the tumor-associated bone relative to untargeted NPs, and also provided benefit through the direct antiresorptive therapeutic function of Aln. The dual benefit of the Aln in the BTNPs was supported by the observations that drug-free Aln-containing BTNPs improved bone volume fraction in bone-tumor-bearing mice, while GANT58-BTNPs created better therapeutic outcomes than both unloaded BTNPs and GANT58-loaded untargeted NPs. These findings suggest GANT58-BTNPs have potential to potently inhibit tumor-driven osteoclast activation and resultant bone destruction in patients with bone-associated tumor metastases.

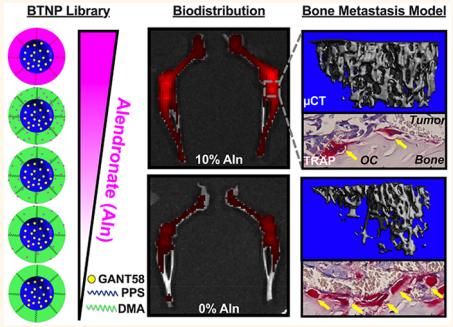

KEYWORDS: *polymer nanoparticles, bone targeting, bone metastasis, tumor delivery, bisphosphonate, pharmacokinetics, hedgehog pathway*

Metastasis is the major prognostic factor for breast cancer patient survival. Breast tumors, in particular, have a propensity to metastasize to bone, with over 70% of patients having bone metastases *post mortem*.[1] Patients presenting with bone metastases often experience significant

Received: June 11, 2019
Accepted: January 2, 2020
Published: January 2, 2020

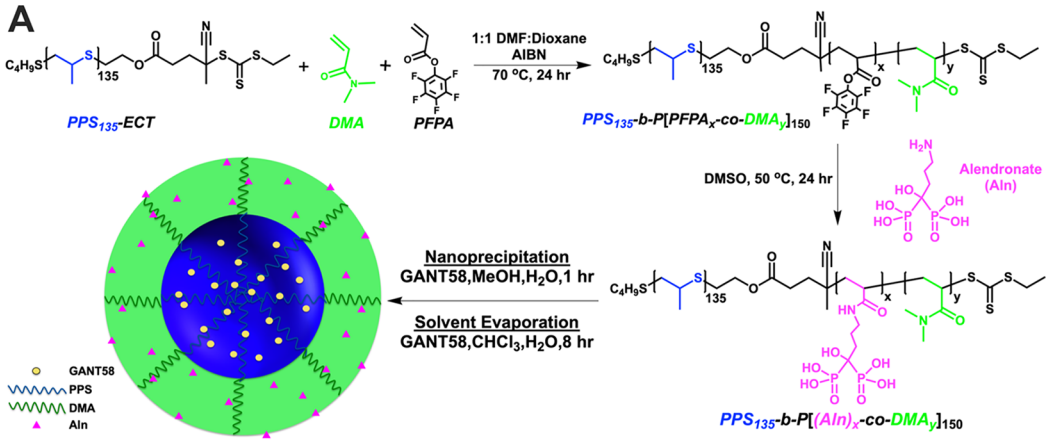

B

% Aln	0	2	5	10	100
Theoretical DP (X/Y)	0/150	3/147	8/142	15/135	150/0
Experimental Aln DP (X)	0	4	6	13	*

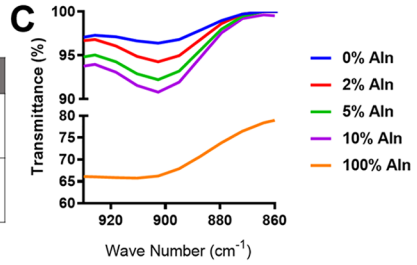

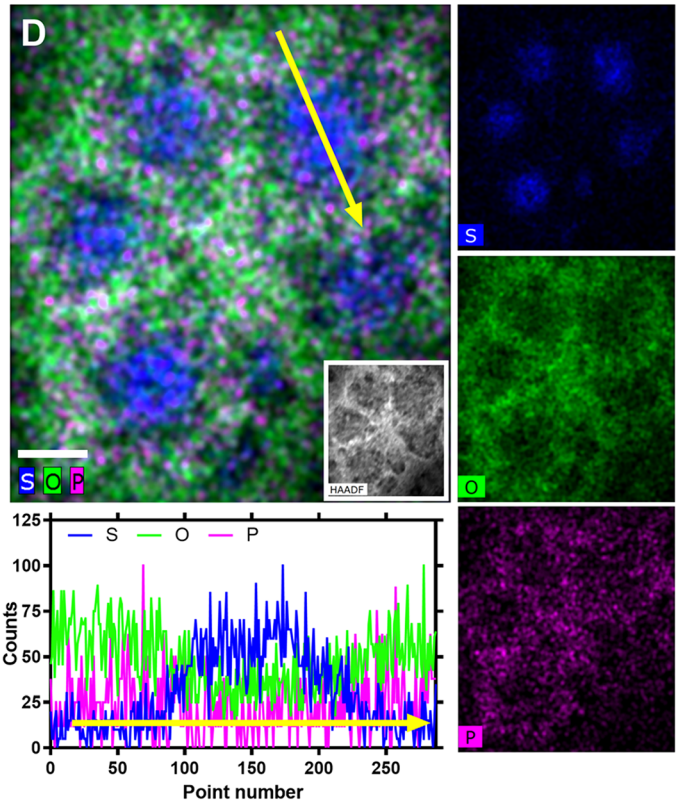

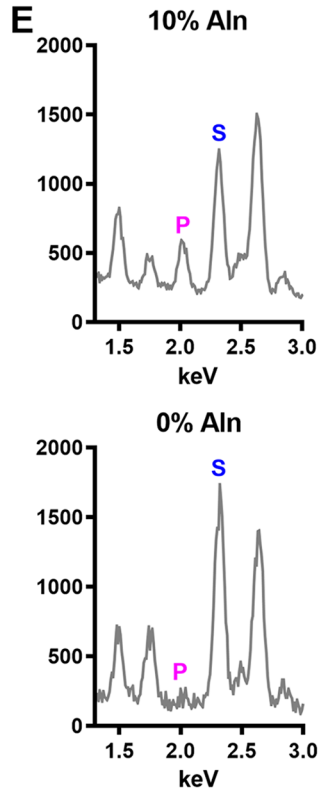

Figure 1. GANT58-BTNP synthesis and characterization validating the BTNP structure. (A) Synthesis of PPS_{135}-*b*-P(Aln-*co*-DMA)$_{150}$ polymer and subsequent BTNP micelle fabrication. (B) Targeted and measured degree of polymerization (DP) of Aln (X, magenta) and DMA (Y, green) in each polymer series. Aln DP measurements are based on spectrophotometric quantification using a cation-chelation competition assay. Resulting BTNPs are denoted by the target % Aln in the hydrophilic, NP surface-forming block (0% Aln, 2% Aln, 5% Aln, 10% Aln, 100% Aln). *Due to a lack of certainty in the MW of 100% Aln polymer resulting from insolubility in the GPC solvent, we refrain from estimating the Aln DP of 100% Aln polymer. However, the 100% Aln polymer contains ~10× the moles of Aln per mass of polymer than the 10% Aln polymer per the competition assay. (C) FTIR spectrum of BTNP polymers. Characteristic P-O bond peak at 910 cm^{-1} indicates varying Aln content. (D) STEM-EDS characterization of 10% Aln formulation using chemical mapping and EDS line scan over the length of a single micelle (yellow arrow, analysis on bottom left). Sulfur (blue), oxygen (green), and phosphorus (magenta) were used as signatures for PPS, DMA+Aln, and Aln,

https://dx.doi.org/10.1021/acsnano.9b04571
ACS Nano 2020, 14, 311−327

Figure 1. continued

respectively. Scale bar: 30 nm. (E) EDS spectra of 10% Aln and 0% Aln formulation, highlighting the consistent sulfur (S, component of PPS) and different phosphorus (P, component of Aln) peak magnitudes.

skeletal complications such as bone pain, increased risk of pathological fracture, and a reduction in mobility that significantly reduces patient quality of life.[2] Current treatment strategies for tumor-induced bone disease (TIBD) include antiresorptives such as bisphosphonates and the RANKL inhibitor, denosumab. These agents systemically inhibit osteoclast activity to reduce bone resorption, which at high doses can be associated with disrupted bone homeostasis at nontumor sites.[3−5] Thus, improved treatments for TIBD that more potently and selectively target tumor-induced bone destruction while limiting off-target effects are needed. We seek to accomplish this goal using a polymeric nanoparticle (NP) carrier to deliver the Gli2 inhibitor, GANT58, which previous data suggest will target tumor-associated, but not physiological, osteoclast function.[6,7]

After metastasis to bone, breast cancer cells disrupt normal bone homeostasis to initiate a vicious cycle of TIBD.[8] Tumor cells in the bone microenvironment secrete parathyroid hormone-related protein (PTHrP) which upregulates osteoblast expression of receptor activator of nuclear factor kappa-B ligand (RANKL), driving subsequent osteoclast activation and resorption of the bone matrix. Bone breakdown releases stores of matrix-bound growth factors, including transforming growth factor beta (TGF-β), that further stimulate tumor growth and osteolytic bone destruction, propagating the cycle.[9] We hypothesize that the small molecule GANT58, which blocks activity of the transcription factor Gli2 and consequent PTHrP expression by tumor cells,[7] will disrupt the vicious cycle and reduce tumor-driven bone resorption. Importantly, Gli2 is primarily associated with development and it is not believed to be involved in normal bone or other tissue function in adults.[10,11] Due to the hydrophobicity and insolubility of GANT58, we developed a colloidally stabilized GANT58 in a systemically deliverable, bone-targeted nanoparticle (BTNP) formulation.

Using this approach, we sought to develop a stable, long-circulating NP with desirable pharmacokinetics (PK) for tumor distribution while also conferring bone binding for superior drug retention at sites of TIBD. Bone targeting of nanomedicines in previous studies has been achieved using bisphosphonates,[12−19] anionic peptides,[20−23] carboxylic acids,[24] and other phosphate-containing moieties.[25] Anionic charge is a consistent characteristic of these bone-targeting ligands, and it can be a challenge to achieve the ideal density of negative charge to bind bone while maintaining sufficient PK and tumor distribution. NPs with highly negative surface charge frequently show poor PK due to scavenger receptor-based removal by macrophages of the reticuloendothelial organs such as liver.[26] Previously, in an application unrelated to bone targeting, Xiao *et al.* showed that NPs with zeta-potentials of −27, −18, −9, +4, +19, +30, and +37 mV produced tumor/liver ratios of 0.82, 1.28, 1.75, 1.18, 0.84, 0.60, and 0.40, respectively.[27] To design and optimize a nanocarrier that addresses this trade-off, we built from our previous work on reactive oxygen species (ROS)-responsive poly(propylene sulfide) core NPs.[28−31] We created a library of BTNPs with tunable density of bone-targeting ligand in an effort to balance systemic PK and tumor accumulation with bone binding and retention properties. The bone-binding bisphosphonate, alendronate, was used as the targeting ligand because it has the potential to improve bone targeting of GANT58, while simultaneously reducing TIBD through the osteoclast inhibitory activity of the bisphosphonate. Previous work comparing bone-targeting ligands has also shown that bisphosphonates exhibit a higher binding affinity than carboxylates and phosphonic acid both *in vitro* and *in vivo*.[32,33] More recent work demonstrated that bisphosphonate conjugation to NPs for targeted chemotherapy delivery can contribute to reduced osteolysis in TIBD,[34] but this team did not study bisphosphonate NP surface density or its PK or pharmacodynamic (PD) consequences. The effect of bisphosphonate ligand density on bone binding has been explored *in vitro*, where it was found that a plateau in *in vitro* bone binding was observed when NPs with >20% of the NP surface were grafted with bisphosphonate, and thus 20% surface coverage was chosen for *in vivo* studies.[12] However, these formulations were not tested to understand how ligand density affects *in vivo* PK/PD. Furthermore, coupling bisphosphonate targeting with delivery of a TIBD inhibitor such as GANT58 to improve bone protection from TIBD has not been investigated. Here, we studied the effect of ligand density on bisphosphonate-conjugated NPs, both for *in vitro* bone binding and for *in vivo* systemic PK, and investigated the dual benefit of GANT58 and bisphosphonate therapy in TIBD as enabled by highly controlled polymer chemistries.

RESULTS AND DISCUSSION

Synthesis of Bone-Binding Diblock Copolymers with Varied Alendronate Content. Five diblock copolymers were synthesized comprising a nanocarrier core-forming block of polypropylene sulfide (PPS) with a degree of polymerization of approximately 135 (10 kDa). PPS can efficiently encapsulate hydrophobic small molecules and elicits negligible toxicity upon systemic administration, motivating its selection as the hydrophobic block.[28−31,35−37] Further, PPS is responsive to ROS, which is prevalent in inflamed tissues such as tumors.[38,39] The sulfide group in PPS reacts with ROS such as hydrogen peroxide to create sulfoxides and sulfones. This reaction causes a phase transition of the polymer from hydrophobic to hydrophilic, resulting in disassembly of the micelle and subsequent cargo release.[40] The PPS block was synthesized *via* anionic ring-opening polymerization and conjugated to the reversible addition−fragmentation chain transfer (RAFT) chain transfer agent (CTA) 4-cyano-4-(ethylsulfanylthiocarbonyl)-sulfanylpentanoic acid (ECT) as previously described to create the RAFT macro-CTA PPS_{135}-ECT (Figure S1).[28,29,35]

The PPS_{135}-ECT was then RAFT polymerization chain extended with a second hydrophilic block consisting of a random copolymer of *N*,*N*-dimethylacrylamide (DMA) and pentafluorophenyl acrylate (PFPA) as an intermediate, which was subsequently reacted with bone-binding alendronate (Aln), yielding PPS_{135}-*b*-P(Aln_x-*co*-DMA_y)$_{150}$ (Figure 1A and Figure S1). DMA was chosen due to its hydrophilicity, low toxicity, and its short pendant chain length so as to not sterically hinder the engagement of the bone-targeting ligand.[41] PFPA was incorporated into the hydrophilic block to act as an amine-

https://dx.doi.org/10.1021/acsnano.9b04571
ACS Nano 2020, 14, 311−327

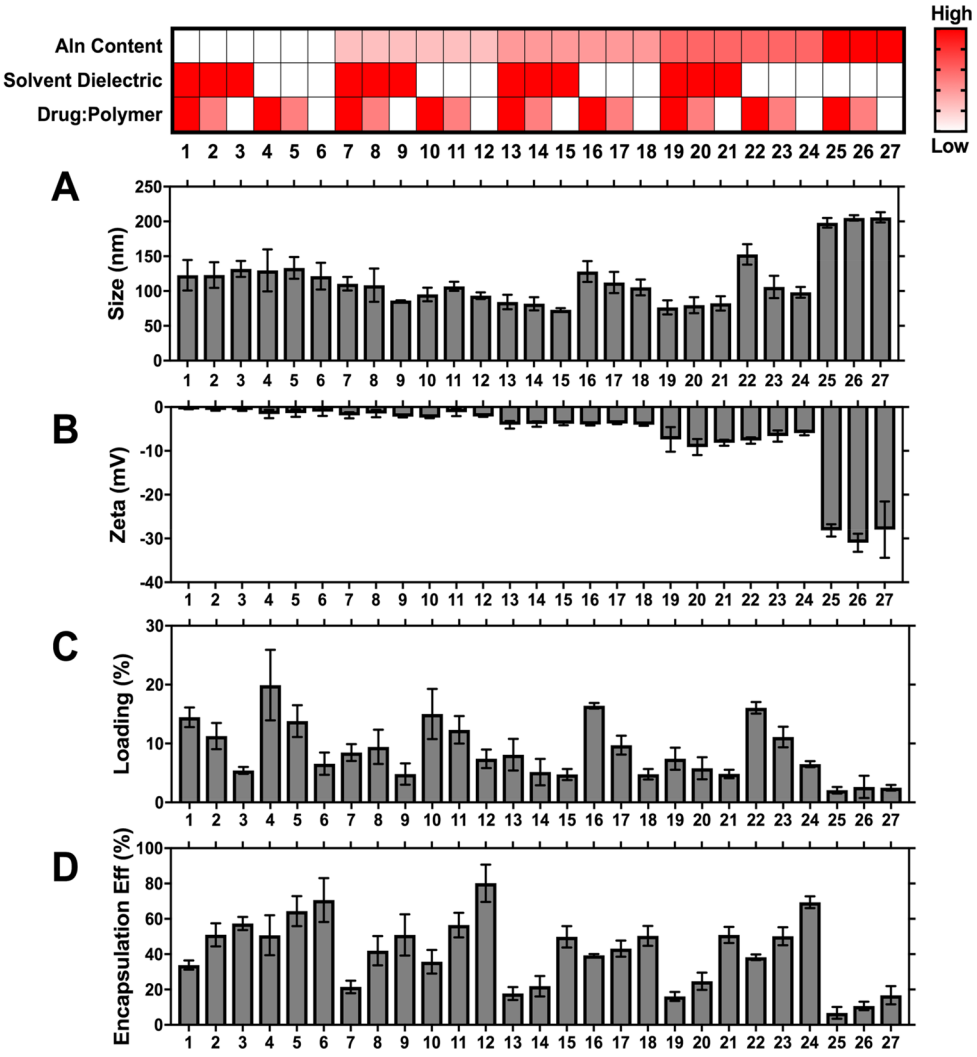

Figure 2. Combinatorial library comparing BTNPs with varying Aln content (0, 2, 5, 10, and 100% Aln), fabrication methods (nanoprecipitation [low solvent dielectric] and solvent evaporation [high solvent dielectric]), and drug/polymer ratios (1:2, 1:4, and 1:10) identifies lead BTNP fabrication conditions. (A) BTNP hydrodynamic diameter and (B) zeta-potential as measured by DLS. (C) BTNP GANT58 loading and (D) encapsulation efficiency.

reactive intermediate for grafting of bone-binding Aln. The DMA and PFPA copolymer was targeted to produce a polymer block with a total degree of polymerization of approximately 150. The stoichiometric ratio of DMA/PFPA in the BTNP surface-forming block was varied to create five diblock copolymer formulations with a target of 0, 2, 5, 10, or 100% PFPA. The primary amine-containing Aln was then grafted *via* the amine-reactive PFPA intermediate to create BTNPs with a target of 0, 2, 5, 10, and 100% Aln in the NP surface-forming polymer block. The concentration of Aln was spectrophotometrically quantified on each BTNP by adapting cation-chelation competition assays that exploit the strong and specific binding of the *o*-cresolphthalein complexone with Ca^{2+}.[42−45] The experimental DP of Aln was found to be within two units of the theoretical DP for the 0−10% Aln polymer series (Figure 1B and Table S1). Fourier transform infrared (FTIR) spectra of the BTNP polymers show a stretching vibration from the P−O bond in Aln at ∼910 cm^{-1}, and an increase in peak intensity with increasing Aln content in polymers indicating Aln content correlated with PFPA content in the parent polymer prior to grafting (Figure 1C and Figure S1E). Aln was chosen as the bone-targeting moiety due to its well-documented bone-binding affinity and its accessible terminal primary amine for reactivity with the PFPA group.[12,13,46,47] Importantly, Aln is also a clinically approved osteoclast inhibitor with the potential to provide BTNP targeting functionality and to contribute to the bone protective outcomes.[3] To generate fluorescently labeled BTNPs, Cy5-amine fluorescent dye was grafted to the PFPA block prior to addition of Aln at a 1:1 fluorophore/polymer molar ratio.

NP Preparation and Morphological Characterization. NPs were fabricated by a bulk solvent evaporation or nanoprecipitation method to create GANT58-loaded PPS_{135}-*b*-P(Aln-*co*-DMA)$_{150}$ bone-targeted nanoparticles (GANT58-BTNPs). Transmission electron microscopy (TEM) was used to confirm that the GANT58-BTNPs assume the expected micellar morphology. TEM images indicated that the GANT58-BTNPs have a spherical morphology and a diameter of approximately 40 nm in their dehydrated form, whereas dynamic light scattering (DLS) showed that they have a hydrodynamic diameter of approximately 100 nm (Figure S2). Chemical mapping using energy-dispersive X-ray spectroscopy (EDS) in scanning TEM (STEM) was used to visualize chemical content of the BTNPs. Sulfur (blue) was used as the chemical signature for PPS, oxygen

https://dx.doi.org/10.1021/acsnano.9b04571
ACS Nano 2020, 14, 311−327

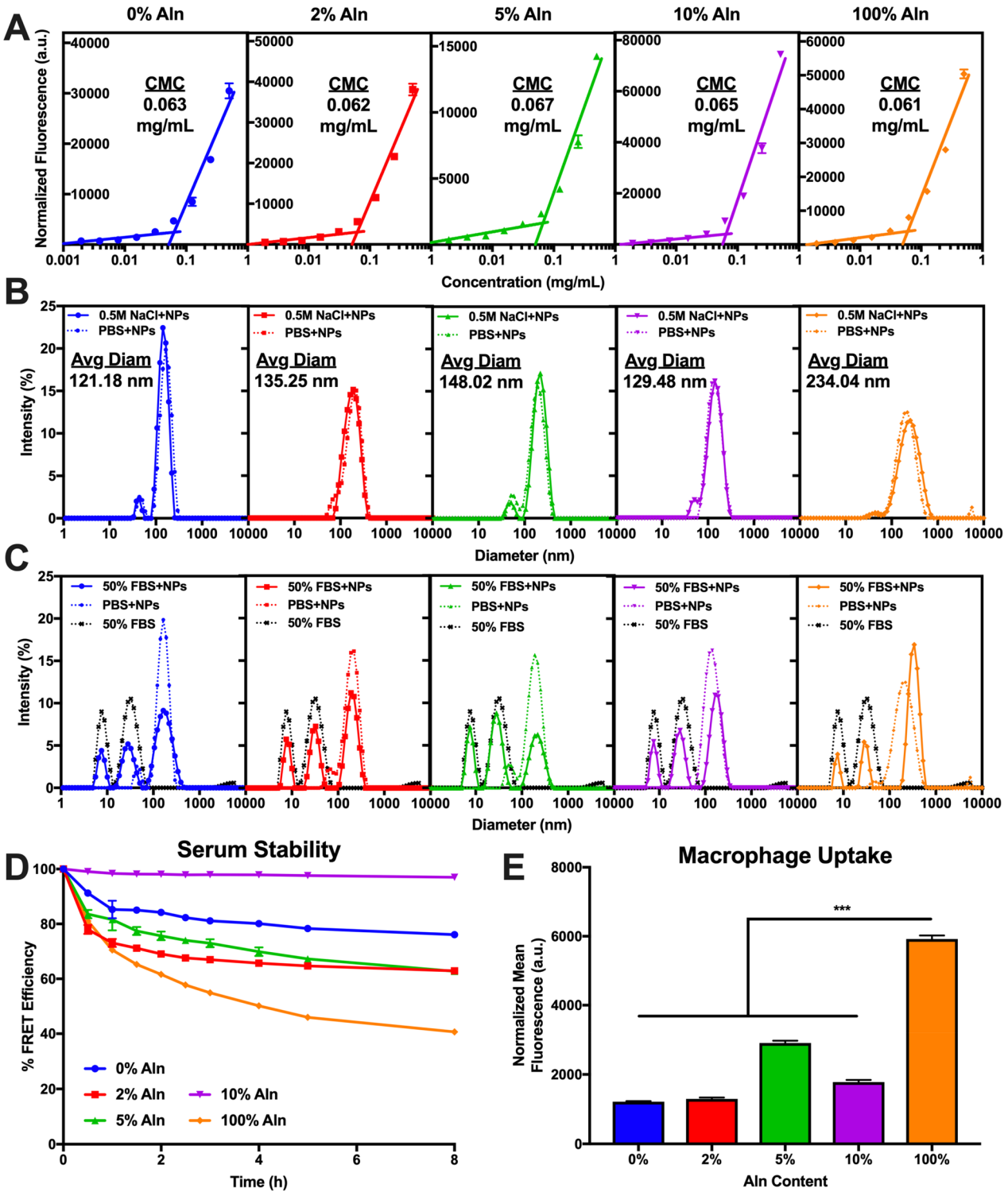

Figure 3. GANT58-BTNP stability and macrophage uptake. (A) Critical micelle concentration of each BTNP formulation as measured by the Nile Red method. (B) Salt stability of BTNPs in high salt concentrations (0.5 M NaCl) as measured by DLS. Serum stability of BTNPs in high serum concentrations (50% FBS) as measured by (C) DLS for NP sizing and (D) FRET for cargo loading stability. (E) RAW 264.7 macrophage uptake of Cy5-labeled BTNPs treated for 3 h and analyzed for cell uptake by flow cytometry.

(green) for DMA and Aln, and phosphorus (magenta) for Aln. Using these chemical signatures, the BTNP morphology was shown to have a sulfur-rich core and a corona rich in oxygen and comprising sparse amounts of phosphorus, suggesting random integration of the Aln into the BTNP surface-forming polymer block (10% Aln shown, Figure 1D). Further, the EDS spectra demonstrate that the 10% Aln formulation has a notable phosphorus peak, whereas the 0% Aln formulation (Figure S3) does not (Figure 1E). The phosphorus signature is indicative of successful Aln grafting.

BTNP Preparation of a Combinatorial Library. Using the five polymers with varied Aln grafting density, two fabrication

https://dx.doi.org/10.1021/acsnano.9b04571
ACS Nano 2020, 14, 311−327

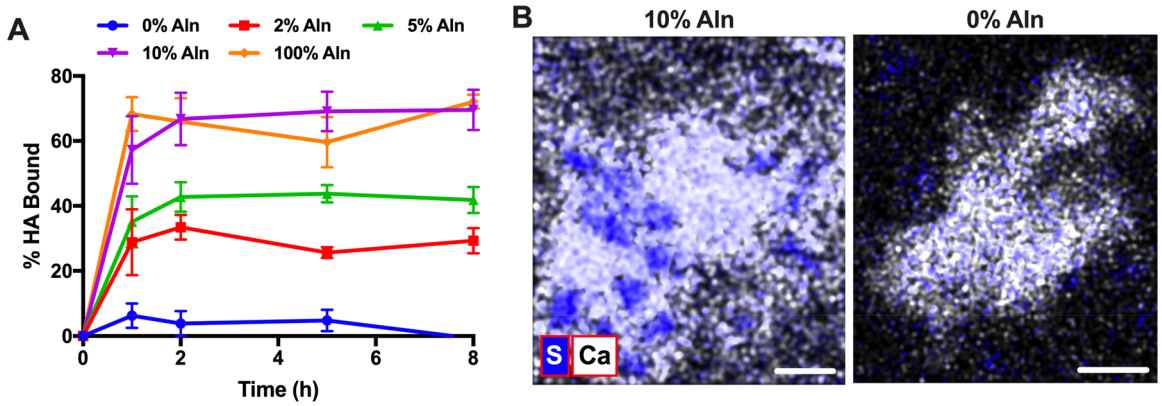

Figure 4. GANT58-BTNPs demonstrate binding affinity to hydroxyapatite. (A) BTNP nHA binding kinetics. NR-loaded BTNPs were incubated with nHA, and percent BTNPs bound to nHA was measured by loss in Nile Red fluorescence in the supernatant over time. (B) Chemical mapping in STEM-EDS enables visualization of 10% Aln BTNPs physically bound to nHA using sulfur (blue) as a chemical signature for BTNPs and calcium (white) as signature for nHA. 0% Aln formulation demonstrates minimal nHA binding. Scale bar: 60 nm.

methods, and varying drug/polymer ratios, a BTNP library was created to identify an optimal formulation based on size, zeta-potential, and drug loading (Figure 2). The hydrodynamic diameter and zeta-potential of the BTNPs were assessed by DLS, and GANT58 loading was measured by GANT58 fluorescence (ex. 485 nm, em. 590 nm) after 2× dilution in dimethylformamide (DMF). GANT58-BTNPs of all polymer formulations exhibited hydrodynamic diameters of approximately 100 nm except the 100% Aln formulation, which exhibited a larger diameter of approximately 200 nm (Figure 2A). BTNPs formed by the nanoprecipitation method were smaller than those made with the solvent evaporation method (96.9 ± 23.5 and 115.1 ± 21.6 nm, respectively, $p < 0.001$), and drug loading had no significant effect on particle size. The surface charge of the BTNPs, as measured by zeta-potential, was Aln-content-dependent, as anticipated. Increasing Aln content yielded BTNPs with more negative surface charge due to the constituent phosphate groups in Aln (Figure 2B). GANT58 was predissolved in the organic phase prior to BTNP fabrication runs at drug/polymer mass ratios of 1:2 (high), 1:4, and 1:10 (low), and resultant BTNP GANT58 loading and encapsulation efficiencies were measured (Figure 2C,D). The average loading and encapsulation efficiencies were significantly higher ($p < 0.001$) in BTNPs synthesized *via* the solvent evaporation method (low solvent dielectric) across all drug/polymer ratios. We surmised that despite the marginally smaller size of the nanoprecipitation-prepared BTNPs, the increased GANT58 loading achieved in the BTNPs prepared by solvent evaporation rendered it the optimal fabrication method. Previous work has shown that NPs of 110 nm have higher tumor/liver ratio than those of 70 or 150 nm, further supporting our hypothesis that the solvent evaporation BTNP formulation is a favorable size for tumor delivery.[48] Thus, we prepared BTNPs *via* the solvent evaporation method for all subsequent experiments. Other studies have demonstrated the utility of developing combinatorial NP libraries using NP characterization techniques and *in vitro* screening to identify optimal NP formulations for use *in vivo*.[49,50] Here, the development of a combinatorial BTNP library facilitated identification of the fabrication approach to be used for *in vivo* studies based on BTNP size, surface charge, and drug loading.

BTNP Stability and Macrophage Uptake. NP *in vivo* bioavailability is essential to maximizing NP accumulation in tumor-associated bone. Dilution of the NPs upon systemic administration can lead to NP disassembly due to NP concentration dropping below the critical micelle concentration (CMC).[51,52] To confirm the CMC of the BTNPs was lower than the initial BTNP blood levels, the CMC was determined by the Nile Red (NR) method (Figure 3A).[28] The BTNPs were determined to be approximately 0.065 mg/mL for all BTNP formulations, which is approximately 1 order of magnitude lower than the BTNP concentration upon intravenous (i.v.) administration (~0.5 mg/mL). Each BTNP formulation was also stable in high salt concentrations (0.5 M NaCl) as measured by DLS, suggesting that the combination of electrostatic and steric repulsion from the P(Aln-*co*-DMA) BTNP corona provides resistance to salt destabilization (Figure 3B). BTNP serum stability was also investigated by measuring both NP size and drug retention when challenged with high serum (50% fetal bovine serum, FBS) conditions. DLS measurements showed that BTNP size was largely unaffected by serum incubation except for 100% Aln, for which the average size increased from ~210 to ~330 nm upon serum exposure (Figure 3C). We hypothesize that this is due to opsonization of serum proteins to the negatively charged surface (−35 mV) of the 100% Aln corona, which may cause particle aggregation. To measure model drug retention in the presence of serum, the Förster resonance energy transfer (FRET) pair DiI and DiO were coloaded into BTNPs and incubated in 50% FBS (Figure 3D). We found that drug retention was dependent on Aln content in the hydrophilic block, with the 100% Aln formulation exhibiting the fastest loss of encapsulated cargo, further demonstrating the instability of this formulation in serum conditions. Incubation of BTNPs in lower FBS concentrations (0, 10, 25% FBS) resulted in similar yet less pronounced trends, with the BTNPs exhibiting high stability in saline (0% FBS) conditions (Figure S4). Notably, the 10% Aln formulation exhibited the highest stability among all formulations.

NP clearance is often initiated *in vivo* by uptake into the mononuclear phagocytic system.[53] Thus, macrophage uptake can be used as a preliminary screen for NP clearance and PK *in vivo*.[49,54] *In vitro* macrophage uptake experiments showed that the 100% Aln BTNPs exhibit macrophage uptake significantly higher than that of the lower Aln content formulations (Figure 3E). Interestingly, the 10% Aln formulation exhibits significantly less uptake than the 5% Aln and 100% Aln formulations. This result aligns with the drug retention findings that showed the 10% Aln is more stable in serum than the other Aln formulations.

https://dx.doi.org/10.1021/acsnano.9b04571
ACS Nano 2020, 14, 311−327

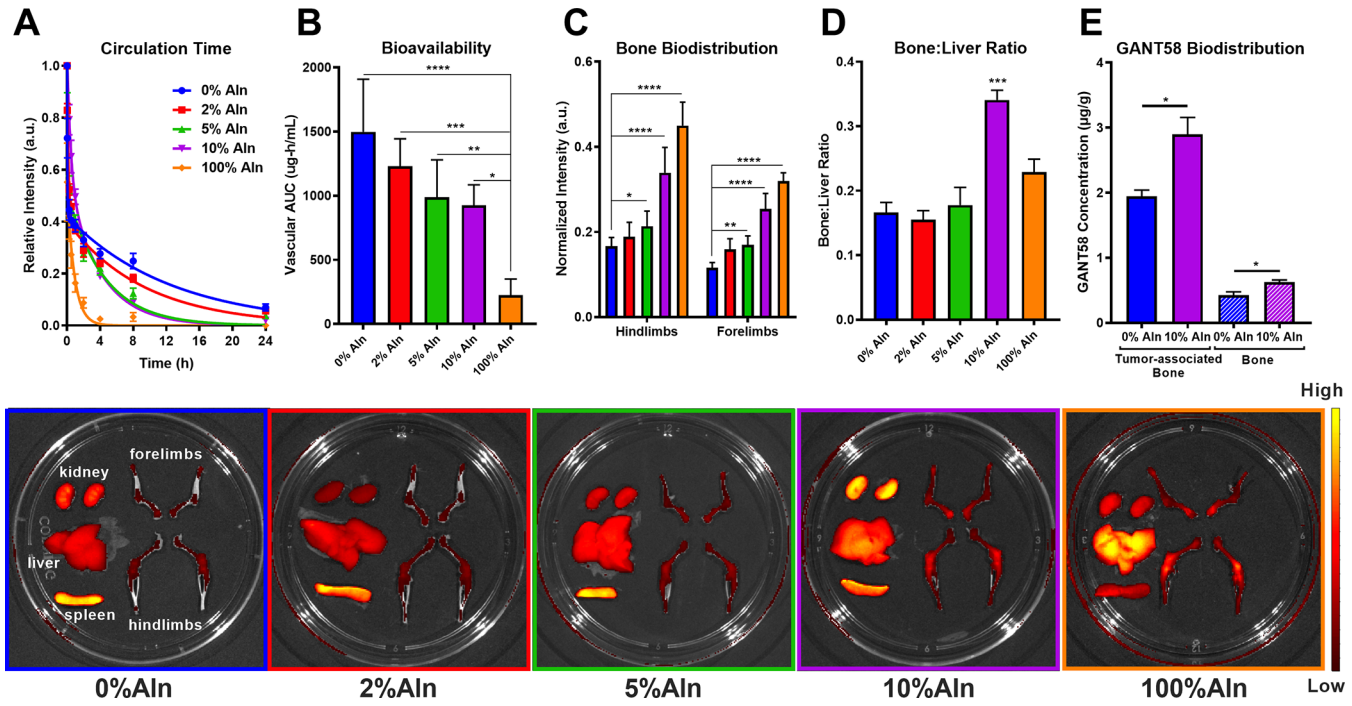

Figure 5. GANT58-BTNP PK and biodistribution indicate that 10% Aln provides an ideal balance of bone binding and vascular bioavailability associated with reduced liver clearance. (A) Circulation time of Cy5-grafted BTNPs as assessed by a tail-nick method. (B) Area under the curve measurements calculated by integration of circulation time curves. (C) Cy5 fluorescence quantification of GANT58-Cy5BTNP distribution to bone 24 h (representative images below). (D) Bone/liver ratios quantified by Cy5 fluorescence at 24 h after injection. (E) GANT58 biodistribution in tumor-associated bone and non-tumor-bearing bone after 10% Aln-GANT58 and 0% Aln-GANT58 BTNPs i.v. administration as assessed by HPLC.

We hypothesize that the combination of steric and electrostatic repulsion in the 10% Aln formulation (zeta-potential: −8 mV) leads to improved drug retention and shielding from macrophage uptake. Other studies have shown that slightly anionic micelles avoid nonspecific organ uptake and improve tumor/liver biodistribution; and a surface charge between 0 and −15 mV leads to minimal macrophage uptake and longer circulation times.[26,27,55,56]

Bone Targeting and Release Characterization of BTNPs. The bone-binding kinetics of the BTNPs were assessed *in vitro* using nanocrystalline hydroxyapatite (nHA) as a bone substitute. An Aln-dependent binding of BTNPs to nHA was observed, with increasing Aln content leading to higher equilibrium nHA binding (Figure 4A). Notably, at these conditions, the 10% Aln formulation exhibited binding kinetics similar to those of the 100% Aln formulation. Adsorption isotherm experiments also demonstrated a similar trend with increasing Aln content leading to greater binding affinity (Figure S5). This finding, along with the results from the combinatorial NP library and the stability studies, supported the use of the 10% Aln BTNP formulation as our lead candidate for subsequent *in vivo* studies. After incubation with nHA, 10% Aln and 0% Aln formulations were further investigated for nHA affinity using chemical mapping in EDS-STEM. Sulfur (blue, indicative of PPS) and calcium (white) were used as the chemical signatures for BTNPs and nHA, respectively. Ten percent Aln BTNPs exhibited significant binding to nHA, whereas the 0% Aln BTNPs showed no specificity or binding to nHA (Figure 4B and Figure S6). The ROS-sensitive behavior of the BTNPs was investigated *in vitro* using H_2O_2 as the representative ROS species and Nile Red (NR)-loaded BTNPs. The NR cargo was released in a H_2O_2 concentration-dependent manner with minimal cargo release at low H_2O_2 concentrations (Figure S7). After micelle disassembly *in vivo* through oxidation, it is hypothesized that the resultant hydrophilic polymers will be small enough for renal clearance as proposed for other PPS-based polymer systems.[40]

BTNP Pharmacokinetics. The PK profile of each GANT58-BTNP formulation was determined by measuring the circulation half-life of fluorescently labeled BTNPs. After retro-orbital injection of Cy5-labeled GANT58-BTNPs (GANT58-Cy5BTNPs), a tail nick method was used to obtain small amounts (<5 μL) of blood immediately postinjection (t = 0) and at subsequent times up to 24 h. The blood samples were then measured for Cy5 fluorescence intensity using a fluorescence plate reader. BTNP concentration was then calculated from a standard curve. Circulation time of GANT58-BTNPs was shown to be Aln-content-dependent, with higher Aln content leading to shorter circulation half-lives and lower systemic bioavailability (Figure 5A,B and Table S2). As expected and in line with other literature, highly negative BTNP surface charge increased clearance and consequently reduced circulation time and bioavailability.

BTNP Biodistribution. The biodistribution of GANT58-Cy5BTNPs was next evaluated following i.v. tail vein injection in non-tumor-bearing CD-1 mice. After 24 h, mice were sacrificed and long bones (forelimbs and hindlimbs) and organs were imaged using an IVIS imaging system. IVIS imaging analysis software was used to quantify Cy5 fluorescence intensity in the long bones (Figure 5C). *In vivo* GANT58-Cy5BTNP fluorescence in the hindlimbs and forelimbs was also found to be Aln-content-dependent, with higher Aln content leading to higher Cy5 signal in bone, as expected based on *in vitro* experiments. Further, Cy5 fluorescence intensity in the

https://dx.doi.org/10.1021/acsnano.9b04571
ACS Nano 2020, 14, 311−327

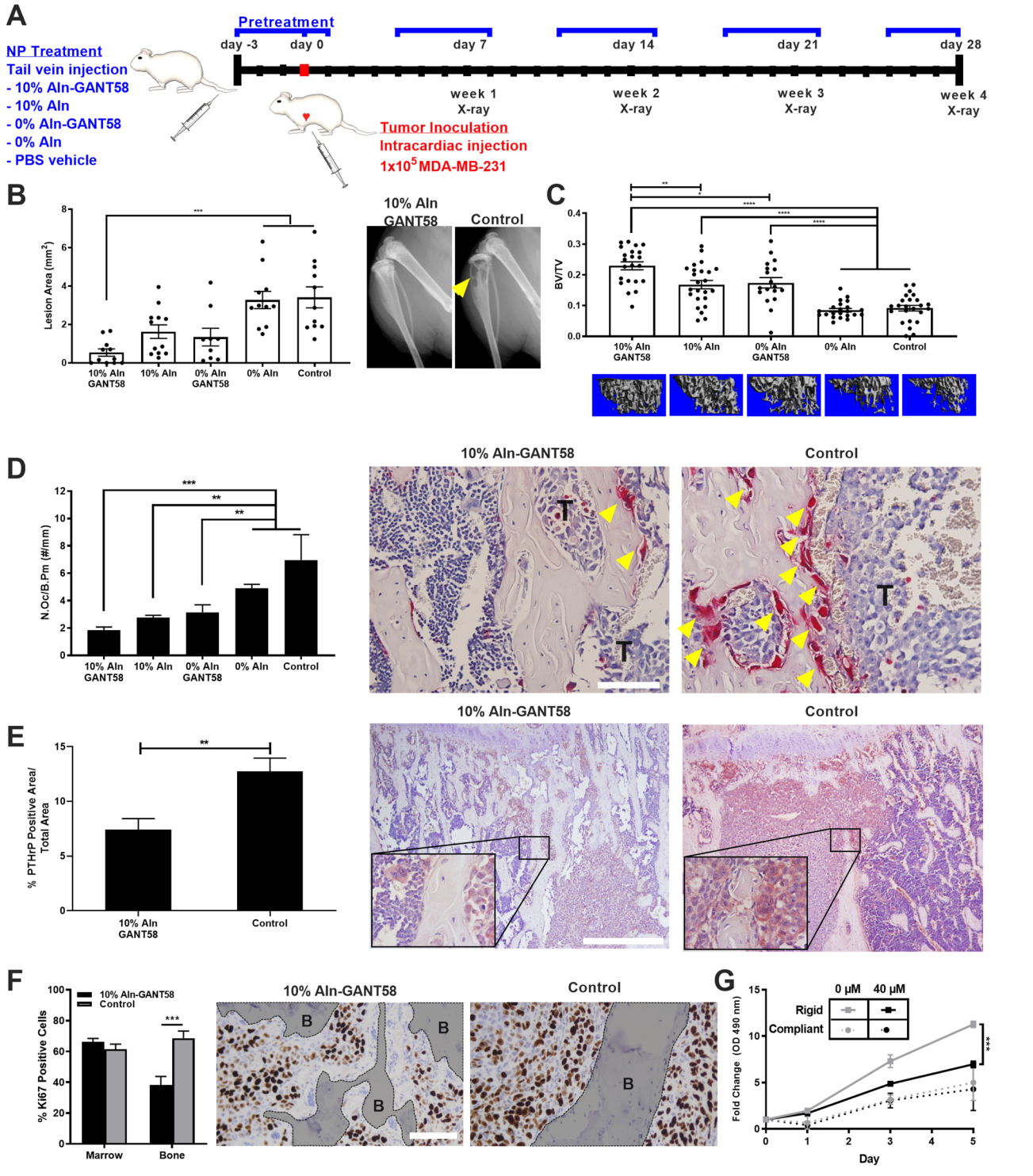

Figure 6. GANT58-BTNP treatment reduces tumor-mediated bone destruction in a mouse model of early bone metastasis. (A) Tumor inoculation and treatment timeline for intracardiac model of bone metastasis. (B) Lesion area as assessed by radiographic analysis of combined hindlimbs is significantly reduced in GANT58-BTNP-treated mice over control ($p < 0.001$). Yellow arrow indicates osteolytic lesions. (C) μCT analysis of tibiae bone volume fraction (BV/TV) showed significantly improved bone preservation in mice treated with GANT58-BTNPs over control ($p < 0.0001$). (D) Tartrate-resistant acid phosphatase histomorphometric analysis of osteoclast (OC) number shows significantly decreased OC number per bone perimeter in GANT58-BTNP-treated mice compared to control ($p < 0.001$). Yellow arrows indicate OCs. Scale bar: 100 μm. (E) PTHrP immunohistochemistry quantification shows that there is a significant decrease in tibial PTHrP protein in mice treated with GANT58-BTNP ($p < 0.01$). Scale bar: 500 μm, inset image 100× magnification. (F) Spatial quantification of Ki67 immunohistochemistry shows that there is a decrease in % Ki67 positive cells at the bone interface when treated with GANT58-BTNPs ($p < 0.001$). Shaded and outlined regions denote bone. Scale bar: 200 μm. (G) *In vitro* MTS proliferation assay over 5 day period after drug treatment shows 40 μM GANT58 treatment slows tumor cell growth on rigid but not compliant substrates ($p < 0.001$).

https://dx.doi.org/10.1021/acsnano.9b04571
ACS Nano 2020, 14, 311−327

forelimbs and hindlimbs was >2-fold higher in mice treated with the 10 and 100% Aln formulation over the 0% Aln formulation. Quantification of bone/liver ratios demonstrates that 10% Aln has a bone/liver ratio significantly higher than that of all other formulations (Figure 5D). Despite the high bone uptake exhibited by the 100% Aln formulation, the 10% Aln formulation was deemed the lead candidate for subsequent studies due to its superior GANT58 drug loading (4-fold higher, Figure 2C), high cargo retention exhibited by FRET studies (Figure 3D), and a smaller, more desirable size for systemic delivery compared to the 100% Aln formulation (100 nm *vs* 210 nm, respectively) and its higher bone/liver biodistrubution ratio (Figure 5D).

Next, visualization of the 10% Aln BTNPs in tumor-bearing mouse tibiae was pursued in order to investigate spatial distribution of the BTNPs within the bone-tumor milieu. MDA-MB-231 bone tumor cells were intratibially injected into mice and allowed 14 days for growth. A single injection of Cy5BTNPs was then administered *via* tail vein injection and allowed 24 h for circulation prior to sacrifice and hindlimb dissection. After cryosectioning, serial sections were stained with hematoxylin and eosin (H&E) or imaged *via* fluorescence microscopy for Cy5 fluorescence. Fluorescence microscopy showed that there was significant Cy5BTNP signal in the tibia after 24 h circulation, and comparison to the H&E section showed that the Cy5BTNPs localized both at the endosteal surface and in the trabeculae, as well as in the tumor space (Figure S8). These findings suggest the BTNPs are able to penetrate the bone matrix and the tumor and are retained there >24 h.

Delivery of the GANT58 cargo to bone and bone-tumor site was determined by high-performance liquid chromatography (HPLC) on tissues extracted from intratibially injected MDA-MB-231 tumor-bearing athymic nude mice that had been systemically treated with GANT58-BTNP (Figure 5E). In mice treated with 10% Aln formulation, GANT58 concentration was approximately 50% higher in both the tumor-associated bone and the non-tumor-bearing bones, indicating that Aln-based bone targeting increases GANT58 concentration at the bone-tumor site. Further, GANT58 biodistribution to the tumor-associated bone was roughly 4-fold higher than that in non-tumor-bearing bone in both groups, suggesting that the enhanced permeation and retention effect contributes to tumor accumulation of NPs through leaky blood vessels[57] at the bone-tumor site.

GANT58-BTNP Treatment Reduces Bone Destruction in a Mouse Intracardiac Model of Bone Metastasis. Based on the *in vitro* and biodistribution studies, it was hypothesized that GANT58-BTNPs could block metastatic tumor-associated bone destruction and potentially reduce initiation of bone metastasis. To test this hypothesis, female athymic nude mice were treated with either GANT58-BTNPs (10% Aln-GANT58, 8 mg/kg GANT58), unloaded BTNPs (10% Aln), nontargeted GANT58-BTNPs (0% Aln-GANT58, 8 mg/kg GANT58), nontargeted unloaded BTNPs (0% Aln), or no treatment control (control) *via* tail vein injection. The inclusion of a free GANT58 arm of the study was precluded by the inability to identify an intravenously tolerable vehicle capable of solubilizing the lipophilic GANT58. MDA-MB-231 bone tumor cells were inoculated *via* intracardiac injection, and treatments were given 5 times/week for 4 weeks (Figure 6A).

Radiographic imaging was used to track tumor progression in the hindlimbs of mice by visualization of osteolytic lesions. Radiographic analysis prior to sacrifice at week 4 showed that the 10% Aln-GANT58-treated mice exhibited smaller and fewer lesions compared to the 0% Aln treated and control mice (Figure 6B and Figure S9). To further assess the bone quality in these mice, microcomputed tomography (μCT) was conducted on the tibiae after sacrifice (Figure 6C). Mice treated with 10% Aln-GANT58, 10% Aln, and 0% Aln-GANT58 had significantly higher bone volume fraction (BV/TV) than the 0% Aln and control mice. These findings demonstrate that the 10% Aln BTNPs alone have a therapeutic effect due to functionalization with the osteoclast-inhibiting bisphosphonate, Aln. This finding aligns with previous studies that have also found that polymer-conjugated Aln exhibits antiresorptive activity *in vivo*.[34,58] Notably, the 10% Aln-GANT58-treated mice exhibited BV/TV significantly higher than that of 10% Aln and 0% Aln-GANT58-treated mice, suggesting that the GANT58 and Aln collaborate to produce better bone outcomes in the setting of TIBD. Measurement of other morphometric parameters including connectivity density (Conn.D), trabecular number (Tb.N), trabecular separation (Tb.Sp), and trabecular thickness (Tb.Th) also demonstrated that 10% Aln-GANT58 treatment significantly improved bone quality (Figure S10). The functional effect of both GANT58 and Aln treatment is to reduce osteoclastogenesis. To confirm that improved bone outcomes with GANT58-BTNP treatment is due to a reduction in osteoclast activation, tartrate-resistant acid phosphatase (TRAP) histological staining was conducted on the tibia samples after μCT analysis (Figure 6D). TRAP staining showed that the 10% Aln-GANT58, 10% Aln, and 0% Aln-GANT58-treated mice exhibited significantly fewer osteoclasts per bone perimeter (N.Oc/B.Pm) than 0% Aln-treated and control mice, with 10% Aln-GANT58 trending toward having the least osteoclasts of any group. The effect of BTNPs on bone cell precursors was next investigated *in vitro* in order to substantiate the *in vivo* study mechanistic finding that GANT58-BTNPs reduce tumor-mediated osteoclastogenesis. First, a coculture of mouse bone-marrow-derived stromal cells and MDA-MB-231 tumor cells was utilized as a means to measure the GANT58-BTNP effect on osteoclastogenesis. The coculture was treated with 40 μM free GANT58, BTNPs, or GANT58-BTNPs and cultured for 7 days prior to fixation and TRAP staining. Results showed that GANT58-BTNP treatment significantly reduced osteoclast number compared to the no treatment control (Figure S11A). These results suggest that GANT58-BTNPs exhibit the hypothesized effect of reducing tumor-mediated osteoclastogenesis.

Previous mechanistic studies have demonstrated that genetic repression of Gli2 transcription factor activity reduces expression of PTHrP and that this is the mechanism that consequently reduces tumor-associated osteoclastogenesis.[59,60] To confirm that this mechanism is operative in the context of GANT58-BTNP treatment, PTHrP immunohistochemistry was carried out as a marker for GANT58-mediated Gli2 inhibition. Quantitation showed that GANT58-BTNP treatment significantly reduced PTHrP protein levels at the bone-tumor site compared to control, suggesting that the reduction in osteoclast number is tied to reduced PTHrP signaling (Figure 6E).

Previous studies showed that Gli2 overexpression accelerates cell cycle progression and augments proliferation in tumor cells, whereas Gli2 inhibition blocks tumor growth *in vitro* and even *in vivo* when Gli2 is molecularly repressed using genetic techniques in bone metastatic cancer cell lines.[60,61] This motivated the hypothesis that blocking Gli activity in metastatic breast tumors could obstruct their potential to establish in bone and adopt a

https://dx.doi.org/10.1021/acsnano.9b04571
ACS Nano 2020, 14, 311−327

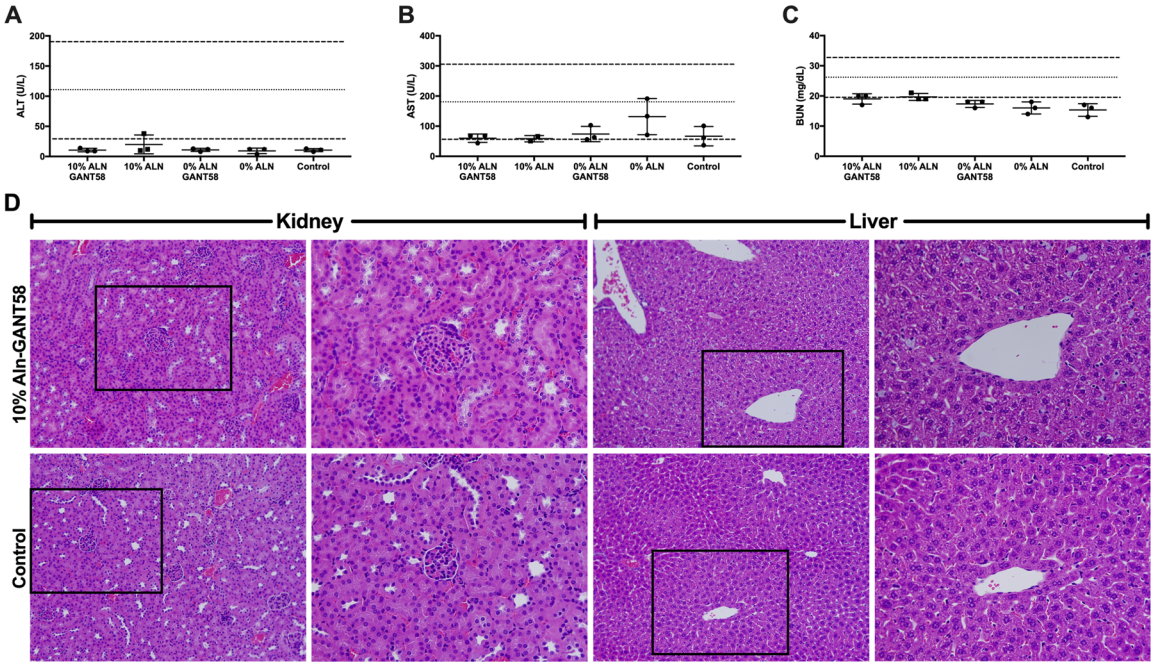

Figure 7. GANT58-BTNPs elicit neglibile systemic toxicity. Biochemical analysis of serum markers of liver toxicity (A) ALT and (B) AST and kidney toxicity (C) BUN after 10% Aln-GANT58, 10% Aln, 0% Aln-GANT58, 0% Aln, or PBS vehicle treatment 5×/week for 4 weeks. Dotted lines indicate two standard deviations above and below reported median levels (dashed line) from animal supplier. (D) Representative images of liver and kidney at 20× and 40× from lead candidate formulation-treated (10% Aln-GANT58) and control mice.

bone-destructive phenotype. However, histomorphometric analysis of the tibiae from treated mice showed no significant decrease in overall tumor burden in 10% Aln-GANT58-treated mice (Figure S12A). It is important to note the large variability in tumor burden inherent to the intracardiac model as evidenced by the large standard error. Even with this variability in consideration, there is significant tumor burden in the 10% Aln-GANT58-treated mice despite maintenance of high bone area (Figure S12B). Based on previous studies from our lab reporting that both mechanically-rigid mineralized bone matrix and TGF-β drive Gli2 expression in bone-metastatic cancer cell lines,[62,63] we hypothesized that GANT58-BTNP treatment may have a spatially heterogeneous effect on tumor cells that mirrors the spatial variation in Gli2 expression. Therefore, we measured the effect of GANT58-BTNP treatment on tumor cell proliferation by measuring Ki67 *via* IHC (Figure 6F). Importantly, we found heterogeneous changes in Ki67 staining, with a reduction of Ki67 positive cells near the bone-tumor interface and more staining away from the bone in the 10% Aln-GANT58-treated mice. However, untreated control mice showed high proliferation rate both at the bone surface and in the tumor space. To further investigate these findings, an *in vitro* proliferation assay was conducted on MDA-MB-231 cells cultured on rigid, tissue culture plastic or compliant gelatin methacrylate (GelMA) gels treated with GANT58 (Figure 6G). The proliferation assay supported the *in vivo* findings showing that GANT58 significantly reduced proliferation of cells on rigid substrates but not on compliant substrates. Taken together, these findings support the concept that concentrated bone surface delivery of the GANT58-BTNP strongly blocks both aberrant osteoclast activation and tumor cell in-growth into the mineralized phase of tumor-containing bone.

Cells respond differently based on the mechanical rigidity of their microenvironment.[64] Mechanically sensitive responses in tumors drive phenotypic changes that alter gene expression and cell behavior causing spatial heterogeneity within the tumor site, especially for a tumor microenvironment that contains both a rigid, mineralized bone phase and soft bone marrow. Previous research in our lab demonstrated that Gli2 expression in bone metastatic cell lines is driven by matrix rigidity,[62,63] and here, we show that Gli2 inhibition has direct tumor cell growth inhibition effects at the mineralized bone interface. Collectively, these findings suggest that GANT58-BTNP effectively protects against TIBD by inhibiting the positive feedback signaling between tumor and bone cells, consequently reducing osteoclast activity, and reducing the stimulation for tumor cells to grow into the mineralized phase of the bone.

Toxicological safety of the GANT58-BTNPs after treatment at therapeutic doses is key to clinical translatability. The toxicological profile of the GANT58-BTNPs was examined by drawing blood at the time of sacrifice for the cohort of mice in the intracardiac model study after having received 10% Aln-GANT58, 10% Aln, 0% Aln-GANT58, 0% Aln treatment, or no treatment control daily at 8 mg/kg GANT58 (or equivalent dose of unloaded BTNPs) for 4 weeks. Biochemical analysis of blood serum markers for liver (ALT and AST) and kidney (BUN) toxicity showed there was no significant increase above two standard deviations from average levels reported by the animal supplier (Envigo) (Figure 7A–C). Further, histological sections showed no evident toxicity in the liver and kidneys of lead candidate formulation-treated mice compared to control (Figure 7D). These findings are consistent with previous studies using PPS-based polymers that have demonstrated toxicological safety even at high NP doses and in non-human primates.[35,65] In addition to systemic toxicity, it is also important that GANT58-BTNPs do not affect normal osteoblastogenesis. To test this, hMSCs were treated with 40 μM free GANT58, BTNPs, or GANT58-BTNPs, and the effect of hMSC differentiation toward osteoblasts was tested using an Alizarin Red mineralization assay. After 14 days culture in osteogenic media, Alizarin

https://dx.doi.org/10.1021/acsnano.9b04571
ACS Nano 2020, 14, 311–327

Red staining showed that the GANT58-BTNP and control treatments had no negative effect on hMSC differentiation and mineralization (Figure S11B).

The current clinical TIBD treatments—bisphosphonates and the RANKL inhibitor denosumab—have been linked to side effects such as osteonecrosis of the jaw (ONJ) and atypical femoral fractures.[66−69] Thus, alternative treatments that mitigate off-target effects are warranted. The low systemic toxicity elicited by GANT58-BTNPs in addition to its efficacy and specificity in inhibiting tumor-induced bone destruction and tumor proliferation at the bone interface highlights the potential benefit of this treatment over gold standard treatments.

CONCLUSION

Synthesis of BTNP polymers and development of a combinatorial NP library yielded a GANT58-loaded lead candidate formulation that significantly reduced bone destruction in an intracardiac mouse model of bone metastasis. The lead BTNP formulation, 10% Aln, demonstrated an ideal balance of systemic bioavailability, tumor biodistribution, and bone-binding affinity. Although conferring bone-binding affinity to NPs is an area of active research,[13,46,70] much of this work focuses on delivery of traditional chemotherapeutics (doxorubicin, paclitaxel, and cisplatin).[15,21,34,58] The bone marrow microenvironment is extremely sensitive to chemotherapeutics, so targeting these chemotherapies specifically to bone with the goal of minimizing off-target effects can lead to significant toxicity to healthy bone cells and bone itself.[71,72] Importantly, the lead formulation here elicited minimal systemic toxicity upon i.v. administration with an aggressive treatment schedule. Further, the application of highly controlled RAFT-based chemistry allowed us to tune the targeting ligand content in order to demonstrate the functional balance between high bone binding and desirable systemic PK, both of which can contribute to efficient delivery to tumors associated with bone. Interestingly, the lead formulation showed dual benefits, with both the bone-targeting ligand Aln and the loaded therapeutic GANT58 significantly contributing to bone protection outcomes. Finally, this study elucidated through histological analysis that there is a spatial heterogeneity in the GANT58-BTNP effects on tumor cell proliferation, with this therapy specifically blocking growth into and destruction of the mineralized phase of bone. This provides insight into the role that the bone microenvironment plays in driving tumor progression and suggests that targeted GANT58 delivery combined with chemotherapy or molecularly targeted therapy should be investigated to yield treatments that will improve both patient quality of life and survival.

MATERIALS AND METHODS

Cell Lines and Reagents. The human breast cancer cell line MDA-MB-231 was obtained from ATCC, and a bone metastatic variant (MDA-MB-231 bone) generated in our lab was used for all *in vitro* and *in vivo* experiments, as previously published.[73,74] MDA-MB-231 bone cells were maintained in DMEM (Cell-gro) plus 10% FBS (Hyclone Laboratories) and 1% penicillin/streptomycin (P/S; Mediatech). All cell lines are routinely tested for changes in cell growth and gene expression. GANT58 was purchased from Santa Cruz Biotechnology (Dallas, TX, USA), and all other reagents were purchased from Sigma-Aldrich (St. Louis, MO, USA) unless otherwise specified.

Synthesis of Hydroxyl End-Functionalized Poly(propylene sulfide) (PPS_{135}-OH). A terminal hydroxyl end functional poly(propylene sulfide) polymer was synthesized by anionic ring-opening polymerization of the three-membered cyclic propylene sulfide monomer using DBU/1-buthanethiol followed by an end functionalization with 2-iodoethanol. In brief, 1,8-diazabicyclo[5.4.0]undec-7-ene (DBU) (3 mmol, 0.46 g, 0.45 mL) in dry THF (15 mL) was transferred to a heat-dried and nitrogen-flushed 100 mL round-bottomed flask and degassed for 30 min. The flask was submerged into an ice bath, and a degassed solution of 1-butanethiol (1 mmol, 0.122 g, 0.138 mL) in THF (10 mL) was added dropwise at 0 °C. After 30 min, freshly dried, distilled, and degassed propylene sulfide (135 mmol, 9.99 g, 10.56 mL) monomer was added to the reaction mixture, and the temperature was maintained at 0 °C for another 30 min. The polymerization was carried out for another 150 min, quenched by addition of degassed 2-iodoethanol (4 mmol, 0.68 g, 0.311 mL), and stirred overnight at room temperature. The next day, the polymer mixture was filtered to remove precipitated salt, and the filtered solution was concentrated under vacuum. The crude polymer was purified by three precipitations into cold methanol (100 mL) from dichloromethane (10 mL) before being vacuum-dried to yield a colorless viscous polymer. The formation of polymer with a terminal hydroxyl functionality was characterized by ^{1}H NMR and GPC. ^{1}H NMR (400 MHz; $CDCl_3$): δ (ppm) 1.3−1.4 (s, CH_3), 2.5−2.8 (s, −CH), 2.8−3.1 (s, CH_2), 3.72 (q, CH_2-OH) (PPS_{135}-OH, M_n = 9700 g/mol, PDI = 1.32).

Synthesis of Poly(propylene sulfide)-4-cyano-4-(ethylsulfanylthiocarbonyl)sulfanylpentanoic acid (PPS_{135}-ECT). The PPS-based reversible addition−fragmentation chain-transfer macrochain transfer agent was prepared using a Steglich esterification reaction between carboxyl-terminated ECT (RAFT agent) and the terminal hydroxyl groups of the PPS_{135}-OH. To a dried flask, PPS_{135}-OH (6.0 g, 0.6 mmol), ECT (0.628 g, 2.4 mmol), and 4-dimethylaminopyridine (DMAP, 0.021 g, 0.18 mmol) were transferred and dissolved in DCM and degassed for 15 min. To this flask, *N*,*N*′-dicyclohexylcarbodiimide (DCC, 0.495 g, 2.4 mmol) was added and stirred at room temperature for 24 h. The polymer mixture was filtered to remove precipitated dicyclohexyl urea and concentrated under vacuum. The crude polymer mixture was diluted with DCM (10 mL) and subsequently purified by three precipitations into 250 mL of cold methanol. ^{1}H NMR (400 MHz; $CDCl_3$): δ (ppm) 1.35 (t, 3H, −S−CH_2−CH_3), 1.3−1.4 (s, 3H, CH_3), 1.88 (s, −C(CN)−CH_3), 2.4−2.67 (m, 4H, −CH_2−CH_2−S), 2.5−2.8 (broad s, S−CH), 2.8- 3.1 (broad s, 2H, CH_2), 3.34 (q, −S−CH_2−CH_3), 4.2 (t, −OCH_2−CH_2) (PPS_{135}-ECT, $M_{n,GPC}$ = 9900 g/mol, PDI = 1.32).

Synthesis of Poly(propylene sulfide)-*b*-poly(pentafluorophenyl acrylate-*co*-dimethylacrylamide) PPS_{135}-*b*-P($PFPA_x$-*co*-DMA_y)$_{150}$. The diblock copolymer PPS_{135}-*b*-P($PFPA_x$-*co*-DMA_y)$_{150}$ was synthesized *via* RAFT polymerization using AIBN as the initiator at a 5:1 molar ratio of PPS_{135}-ECT to AIBN. In order to minimize PFPA hydrolysis during synthesis, anhydrous solvents were used in all synthesis steps. In a 10 mL round-bottom reaction flask, PPS_{135}-ECT (0.3 g, 0.03 mmol) was codissolved with stoichiometric amounts of PFPA and DMA in 1:1 DMF to 1,4-dioxane (4 mL) to achieve a final second block chain length of 150, where the PFPA amount was varied from 0 to 100% PFPA in the 150-unit second block with the balance DMA. A solution of AIBN (0.98 mg, 0.006 mmol) in 1,4-dioxane was added to the reaction mixture and degassed for 15 min by bubbling ultra-high-purity nitrogen through the reaction mixture. The reaction flask was then submerged in a 70 °C oil bath and polymerization was allowed to proceed for 24 h. The final polymerization mixture was precipitated twice in cold diethyl ether and dried under vacuum overnight to yield a light-yellow polymer.

Synthesis of PPS_{135}-*b*-P(Aln_x-*co*-DMA_y)$_{150}$ and Fluorescent PPS_{135}-*b*-P(Aln_x-*co*-DMA_y)$_{150}$. The amine-reactive PFPA group of PPS_{135}-*b*-P($PFPA_x$-*co*-DMA_y)$_{150}$ was used to graft alendronate (Aln), an amine-terminated bisphosphonate, to the polymer backbone. PPS_{135}-*b*-P($PFPA_x$-*co*-DMA_y)$_{150}$ (0.013 mmol, 0.3 g), triethylamine (0.013 mmol, 1.8 μL), and Aln (10% excess of PFPA molar content) were added to a dry round-bottom flask and dissolved in DMSO (4 mL) and submerged in a 50 °C oil bath. The amine conjugation was allowed to proceed for 24 h at 50 °C. The reaction contents were then dialyzed against deionized water for 48 h followed by lyophilization. For fluorescent labeling of polymers, Cy5-amine (0.013 mmol) was added to the reaction flask prior to Aln addition and reaction allowed to

https://dx.doi.org/10.1021/acsnano.9b04571
ACS Nano 2020, 14, 311−327

proceed 24 h. To the same reaction flask was added Aln, and the reaction proceeded as described. The resulting polymer was then dialyzed first against methanol for 48 h until disappearance of the fluorophore color and then against deionized water for 48 h.

Fourier Transform Infrared Analysis. To confirm that the synthesized polymers had varied Aln concentrations, FTIR spectra were recorded on a Bruker Tensor 27 system (Billerica, MA). Briefly, Aln and polymers with different percentage of Aln (5 mg) were mixed with IR-grade KBr (100 mg), and pellets were prepared on a KBr press (Specac, Slough, UK). The presence of Aln was identified based on the presence of the stretching vibration of the P−O bond in Aln.[75]

Determination of Aln Content. A fully water-soluble cation-chelation assay adapted from previously established methods was developed in order to measure the polymer-bound Aln relying on the competitive chelation of Ca^{2+} with the well-established calcium quantification chromagen, *o*-cresolphthalein complexone.[42−45] First, 10.3 mg of *o*-cresolphthalein complexone was dissolved into 100 mL of 0.1 M glycine buffer (pH 10) and was used to dissolve various concentration of Aln (standard curve, 0−2 mM) or Aln-containing polymers. Two hundred microliters of each was added to a well of a 96-well plate, and an absorbance reading was measured at 570 nm. The plate was then removed, and 5 μL of a 1 mM $CaCl_2$ solution was added to each well. The plate was gently shaken for 5 min and the absorbance measured again at 570 nm. Absorbance of the Aln reading with $CaCl_2$ was subtracted by the corresponding well/reading without $CaCl_2$ and used to form a standard curve (R^2 = 0.97−0.99). Different concentrations of the Aln polymer were also used in order to ensure the polymer fell within the linear range of the assay (typically characterized as the region where doubling the polymer concentration resulted in doubling of absorbance difference ($+CaCl_2$ *vs* $-CaCl_2$), corresponding to the 0.1−0.7 mM region of the Aln standard curve). The number of Aln per polymer chain was then estimated based on the molecular weight of the polymer.

GANT58-BTNP Formulation and Characterization. GANT58-loaded nanoparticles (GANT58-BTNPs) were fabricated by either the bulk solvent evaporation method or nanoprecipitation method. PPS_{135}-*b*-$P(Aln_x$-*co*-$DMA_y)_{150}$ and GANT58 were dissolved in chloroform (solvent evaporation) or methanol (nanoprecipitation) and added dropwise to stirring phosphate-buffered saline (PBS, 1 mL). For the solvent evaporation method, the biphasic solution was left stirring overnight to allow for chloroform evaporation and micelle formation. For nanoprecipitation, the solution was allowed to stir for 1 h, after which the methanol was removed from the solution *via* rotary evaporation. The resulting micelle solution was filtered by syringe filtration (0.45 μm cutoff) producing the final GANT58-BTNP formulation. The same technique without GANT58 was used to create empty PPS_{135}-*b*-$P(Aln_x$-*co*-$DMA_y)_{150}$ NPs (Empty-BTNPs). The hydrodynamic diameter (D_h) and zeta-potential (ζ) of the GANT58-BTNPs and Empty-BTNPs was measured by dynamic light scattering at a concentration of 1 mg/mL in PBS (pH 7.4) *via* a Malvern Zetasizer Nano-ZS (Malvern Instruments Ltd., Worcestershire, UK) equipped with a 4 mW He−Ne laser operating at λ = 632.8 nm. TEM samples were prepared as previously described.[35] Briefly, 5 μL of GANT58-BTNPs was pipetted onto a carbon TEM grid (Ted Pella, Inc., Redding, CA, USA), blotted dry after 60 s, and counterstained with 1% uranyl acetate for 20 s, and allowed to vacuum-dry overnight. The grids were imaged on an FEI Tecnai Osiris microscope (Hillsboro, OR, USA) operating at 200 kV for TEM and scanning transmission electron microscopy energy-dispersive X-ray spectroscopy.

The fluorescent properties of GANT58 were used to measure GANT58 loading within the BTNPs. GANT58-BTNPs in PBS (50 μL) were pipetted into a 96-well plate and dissolved by adding an equal amount of DMF. A GANT58 standard curve in the same solvent (1:1 DMF/PBS) was prepared on the same plate. Fluorescence intensity of GANT58 (ex. 485 nm, em. 590 nm) was measured on a microplate reader (Synergy H1, Biotek, Winooski, VT), and GANT58 concentration was calculated from the standard curve. Loading was calculated as mass of GANT58 per total mass of BTNPs (%), whereas the encapsulation efficiency was calculated as the mass of GANT58 in the BTNPs per the mass of GANT58 introduced (%).

Critical Micelle Concentration. The critical micelle concentration was measured as previously described.[28,35] Nile Red was used as the encapsulated cargo due to its hydrophobic fluorescence properties and its similar molecular weight to GANT58. NR is ideal for identifying intact micelles due to its fluorescence in hydrophobic environments and minimal fluorescence in aqueous environments. NR-loaded PPS_{135}-*b*-$P(Aln_x$-*co*-$DMA_y)_{150}$ micelles (NR-BTNPs) were fabricated by solvent evaporation, and serial dilutions of the NR-BTNPs were prepared in PBS. NR fluorescence (ex. 535 nm, em. 612 nm) was then read on a microplate reader (Synergy H1, Biotek, Winooski, VT), and the intersection point on the semilog plot of NR fluorescence *versus* polymer concentration was defined as the CMC as previously described.[28]

BTNP Stability Measurements. BTNP stability was tracked by measuring the BTNP hydrodynamic diameter in salt and serum using DLS. BTNPs were prepared at a concentration of 100 μg/mL in solutions of NaCl (0.5 M) or fetal bovine serum (50% in PBS) and incubated for 2 h prior to DLS measurements. Hydrodynamic diameters were compared to control BTNP solutions prepared in PBS. Serum stability was further investigated using a FRET-based assay described previously.[35,76] Briefly, BTNPs were coloaded with the FRET pair DiI and DiO and incubated in 50% FBS. Fluorescence measurements were taken at emission wavelengths of 517 and 573 nm after excitation at 480 nm over an 8 h time period on a fluorescence microplate reader. FRET efficiency was calculated as

$$\%\mathrm{FRET} = \frac{I_{573}}{I_{573} + I_{517}} \times 100$$

Macrophage Uptake. RAW 264.7 macrophages were seeded at 25 000 cells/well in a 24-well plate. After 24 h, cells were incubated with DMEM containing 1 mg/mL Cy5-grafted GANT58-BTNPs for 4 h. Cells were then washed 3× with PBS containing 1% bovine serum albumin, harvested using a cell scraper, and pelleted. Cell pellets were resuspended in PBS containing 0.04% trypan blue and run through a flow cytometer (BD LSR Fortessa, BD Biosciences, Franklin Lakes, NJ, USA). Cy5 fluorescence (ex. 640, em. 670) was monitored; 1000 cells were collected for each measurement, and mean Cy5 fluorescence was normalized to original BTNP solution fluorescence. Untreated RAW 264.7 cells were used as negative controls.

***In Vitro* Bone-Binding Kinetics.** The bone-binding kinetics of the BTNPs were assessed using nanocrystalline hydroxyapatite (Sigma) as the substitute for bone *in vitro* as described previously.[12,77,78] Briefly, NR-BTNPs were prepared as described and incubated at 1 mg/mL—or at varying concentrations for adsorption isotherm experiments—with 40 mg nHA in 4 mL of PBS. Samples were then placed on a stir plate (Cimarec, Thermo Scientific, Waltham, MA) in a 37 °C incubator. At predetermined time points, samples were centrifuged at 1500 rpm for 5 min and a 100 μL sample of the supernatant was removed and measured for NR fluorescence intensity (ex. 535 nm, em. 612 nm) on a microplate reader (Synergy H1, Biotek, Winooski, VT). NR fluorescence in the nHA-containing supernatant was divided by fluorescence in samples prepared identically but without nHA in order to calculate the fraction of unbound NPs, which was then converted to a percentage and subtracted from 100 to obtain the % HA bound.

Mineralization Assay. Human mesenchymal stem cells (hMSCs) were seeded in a 24-well plate at 50 000 cells/well and allowed to proliferate for 48 h in MSC growth medium 2 (PromoCell) as previously described.[79] Medium was then changed to MSC osteogenic differentiation medium (PromoCell) treated with vehicle (DMSO), free GANT58 (40 μM), BTNPs (10% Aln, 40 μM equivalent polymer dose), or GANT58-NPs (10% Aln-GANT58, 40 μM GANT58) to induce osteoblast differentiation. After 14 days culture with media changes every third day, cells were then washed with PBS, fixed in 10% formalin for 45 min, and stained with Alizarin Red S (80 mM) for 30 min. Cells were then washed 5× with water and observed *via* an inverted microscope. Five percent SDS was then used to extract the Alizarin dye by incubation in the surfactant for 1 h under constant shaking. The extracted Alizarin dye was then read on a plate reader at OD 405 nm.

https://dx.doi.org/10.1021/acsnano.9b04571
ACS Nano 2020, 14, 311−327

Osteoclastogenesis Assay. Mouse bone-marrow-derived stromal cells (BMSCs) were isolated from C57BL/6J mice for use in an osteoclastogenesis coculture assay as described previously.[80,81] Briefly, hindlimbs were dissected, and both ends of the femora and tibiae were cut. BMSCs were collected *via* centrifugation and plated on 100 mm culture dishes in α-MEM. Nonadherent cells were then collected and pelleted after 2 h. The BMSCs (500 000 cells/well) and MDA-MB-231 bone tumor cells (1000 cells/well) were seeded in 48-well plates in 300 μL of media supplemented with 10 ng/mL TGF-β (day 1). On day 1, treatments began with free GANT58 (40 μM), BTNPs (10% Aln, 40 μM equivalent polymer dose), and GANT58-BTNPs (10% Aln-GANT58, 40 μM GANT58). On each subsequent day, medium was replaced with fresh α-MEM supplemented with treatments until fixation on day 6. Cells were fixed, stained for TRAP, and counterstained with hematoxylin using a TRAP kit (Sigma) per the manufacturer's instructions. TRAP-positive cells with more than two nuclei were counted as osteoclasts. An experimental group without MDA-MB-231 bone tumor cells (no tumor) served as a negative control.

Hydrogen Peroxide (H_2O_2)-Dependent Drug Release. The ROS-sensitive behavior of the BTNPs was measured as previously described, using H_2O_2 as the ROS species.[35] Briefly, NR-BTNPs prepared as described were exposed to a range of concentrations (1−2000 mM) of H_2O_2. Fluorescence intensity of NR was monitored in a 96-well plate using a microplate reader (Synergy H1, Biotek, Winooski, VT). NR release caused by BTNP oxidation and destabilization was kinetically measured based on loss in NR fluorescence. The percent NR release was calculated from the NR fluorescence loss in the presences of H_2O_2 by comparing the fluorescence reading from that of the fluorescence value prior to H_2O_2 addition and presented as a percent NR remaining. This value was then subtracted from 100% and presented as percent NR release.

Biodistribution. CD-1 female mice (4−6 weeks old, Envigo, n = 5) were injected with GANT58-loaded Cy5-grafted PPS_{135}-*b*-P(Aln_{15}-*co*-DMA_{135}) (GANT58-Cy5BTNPs) *via* tail vein injection (8 mg/kg GANT58). At 24 h post-NP injection, mice were sacrificed and organs and long bones (forelimbs and hindlimbs) were imaged on an IVIS Lumina III imaging system (Caliper Life Sciences, Hopkinton, MA). ROI analysis was conducted on the images using the IVIS software. For GANT58 biodistribution, female athymic nude mice (4−6 weeks old, Envigo, n = 5) were injected with 2.5 × 10^5 MDA-MB-231 bone tumor cells in 10 μL of PBS into the left tibia under isoflurane anesthesia as previously described.[82] As a control, the contralateral limb was injected with 10 μL of PBS. After 2 weeks for tumor establishment, 10% Aln-GANT58 BTNPS or 0% Aln-GANT58 BTNPs were administered *via* tail vein injection. After 24 h circulation, mice were sacrificed and limbs and organs were flash frozen in liquid nitrogen. Limbs were then cryo-milled (SPEX SamplePrep, Metuchen, NJ, USA) and resulting milled powder was weighed. Liquid−liquid extraction was conducted in a 6:1 DCM/PBS solution, and the DCM layer containing GANT58 was collected. After DCM was removed by vacuum, GANT58 was reconstituted and concentration was measured by HPLC.

Cryohistology. Rag 2−/− mice (female, 4−6 weeks old, n = 3) were inoculated with 2.5 × 10^5 MDA-MB-231 bone tumor cells in 10 μL of PBS into the left tibia under isoflurane anesthesia as previously described.[82] Cy5BTNPs were administered *via* a single tail vein injection, and mice were sacrificed at 24 h. Tibiae were dissected and frozen before being embedded in optimal cutting temperature compound (Fisher Healthcare). Serial sections with a thickness of 5 and 20 μm were collected using the multipurpose cryosection preparation kit from Section-Lab Co. Ltd. (Yokohama, Japan) and fixed in 10% formalin to either be stained with hematoxylin and eosin or used for fluorescent imaging. The 5 μm samples were fixed in 10% formalin for 30 s and rinsed with deionized water. The sections were then stained with hematoxylin solution, Gill No. 3, rinsed with deionized water, stained with Eosin from Section-Lab Co. Ltd., and rinsed again with deionized water. The sections were rinsed with 100% ethanol and then with deionized water before being mounted onto a slide with Prolong Gold mounting media (Thermo Fisher). The 20 μm samples were fixed in 10% formalin for 30 s and rinsed with deionized water. The sections were then mounted onto a slide with Prolong Gold mounting media with DAPI (Thermo Fisher).

Pharmacokinetics. Cy5-grafted GANT58-BTNPs were injected into Rag 2−/− mice (female, 4−6 weeks old, n = 5) *via* retro-orbital injection (8 mg/kg GANT58, 100 μL injection) under isoflurane anesthesia. At 1 min, 15 min, 30 min, 1 h, 2 h, 4 h, 12 h, and 24 h, a small volume of blood (<5 μL) was drawn *via* tail nick, collected in a heparinized capillary tube, and dispensed into PCR tubes. The whole blood samples contained in PCR tubes were then frozen at −80 °C. Samples were thawed at time of analysis, diluted 40× in PBS, and then read on a Take3 microvolume plate (Biotek) in a Synergy H1 fluorescence plate reader (Biotek). Background fluorescence was subtracted using a blank whole blood sample control. A standard curve was made by adding Cy5-grafted BTNPs into mouse blood that was then frozen until time of analysis and was then diluted 40× as were the samples.

Orthotopic Mouse Model of Early Bone Metastasis. Mice (athymic nude, female, 4−6 weeks old, Envigo) were inoculated with 1 × 10^5 GFP-expressing MDA-MB-231 cells *via* intracardiac injection into the left cardiac ventricle while under isoflurane anesthesia, as previously described.[60] Mice were treated 5× per week *via* 100 μL tail vein injections with GANT58-BTNPs (10% Aln formulation, 8 mg/kg, n = 12), GANT58-NPs (0% Aln formulation, 8 mg/kg, n = 12), unloaded BTNPs of the same formulations (10% Aln and 0% Aln, n = 12 per group), or PBS (control). Mice were imaged weekly *via* radiographic imaging to track tumor progression and sacrificed at 4 weeks.

Radiographic Imaging. Starting 1 week post-tumor cell inoculation, mice were imaged *via* radiographic imaging using a Faxitron LX-60. Mice were anesthetized using isoflurane and laid in a prone position on the imaging platform. Images were acquired at 35 kVp for 8 s. Lesion area and number in the combined hindlimbs of the mice were measured using quantitative image analysis software (Metamorph, Molecular Devices, Inc.) by region of interest analysis. All data are represented as mean lesion area and number per mouse.

Microcomputed Tomography. A high-resolution μCT 50 system (Scanco Medical) was used to analyze the mouse tibiae bone volume and microarchitecture. Tomographic images were acquired of hindlimbs in 70% ethanol (70 kVp, 12 μm voxel size, 300 ms integration time). μCT images were reconstructed, filtered (σ = 0.2, support = 1.0), and thresholded at 230. Tibiae were contoured starting 10 slices below the growth plate and continued 100 slices in the distal direction using the Scanco software algorithm. Images of individual tibiae were analyzed using the Scanco Medical Imaging software to determine the morphometric parameters.

Histology/Histomorphometry. At autopsy, tibiae were removed and fixed in 10% formalin (Fisher Scientific) for 48 h at room temperature. Fixed tibiae were then stored at 4 °C in 70% ethanol and subsequently decalcified in 10% EDTA for 2 weeks at 4 °C. Specimens were then embedded in paraffin and sectioned into 5 μm sections *via* microtomy. Bone sections were stained with H&E, orange G, and phloxine and examined under a microscope. Tumor burden in the tibiae was quantified using Metamorph software (Molecular Devices, Inc.) and region of interest analysis. For osteoclast analysis, bone sections were stained for TRAP utilizing a substrate incubation step (0.2 mg/mL Napthol AS-BI) followed by a color reaction (25 mg/mL Pararosaniline dye) to form a bright red stain in TRAP-positive cells. Sections were then counterstained with hematoxylin, coverslipped, and examined under a microscope and quantified using OsteoMeasure software (OsteoMetrics, Decatur, GA, USA). Liver and kidney were also removed during autopsy. Processing, embedding, sectioning, and H&E staining were performed by the Vanderbilt Translational Pathology Shared Resource (TPSR) per established protocols.

Immunohistochemistry. Ki67 immunohistochemical staining was performed by the Vanderbilt TPSR per established protocols. PTHrP immunohistochemistry was carried out as previously described on decalcified paraffin-embedded tibial sections using a rabbit anti-PTHrP antibody (1:2500, R87).[83,84] Metamorph software (Molecular Devices, Inc.) was used to quantify PTHrP-positive staining.

https://dx.doi.org/10.1021/acsnano.9b04571
ACS Nano 2020, 14, 311−327

Proliferation Assay. In a 96-well plate, MDA-MB-231 bone tumor cells were seeded at 2000 cells/well in triplicate. Half of the wells were precoated with 0.5 mm GelMA as a compliant substrate. Vehicle (DMSO) or GANT58 (40 μM) was added to wells after 24 h. Cell proliferation was determined by MTS assay using the CellTiter 96 aqueous nonradioactive cell proliferation assay kit (Promega) per the manufacturer's instructions. Absorbance values were measured at OD 490 nm on a plate reader and normalized to no cell controls in the respective GelMA-coated and uncoated wells.

Ethics Statement. All animal protocols were approved by Vanderbilt University Institutional Animal Care and Use Committee (IACUC) and were conducted according to National Institutes of Health (NIH) guidelines for care and use of laboratory animals.

Statistical Methods. Unless otherwise stated, statistics were determined via a one-way ANOVA with Tukey multiple comparisons test using Prism 7 software. All reported data display mean and standard error unless otherwise noted. A value of $p < 0.05$ was considered statistically significant with $n \geq 3$ for all experiments.

ASSOCIATED CONTENT

Supporting Information

The Supporting Information is available free of charge at https://pubs.acs.org/doi/10.1021/acsnano.9b04571.

Further polymer characterization, *in vitro* BTNP behavior, pharmacokinetic parameters and mouse model results (PDF)

AUTHOR INFORMATION

Corresponding Author

Craig L. Duvall − *Vanderbilt University, Nashville, Tennessee;* orcid.org/0000-0003-3979-0620; Email: craig.duvall@vanderbilt.edu

Other Authors

Joseph Vanderburgh − *Vanderbilt University, Nashville, Tennessee, Vanderbilt University Medical Center, Nashville, Tennessee, and Tennessee Valley Healthcare System, Nashville, Tennessee*

Jordan L. Hill − *Vanderbilt University, Nashville, Tennessee*

Mukesh K. Gupta − *Vanderbilt University, Nashville, Tennessee*

Kristin A. Kwakwa − *Vanderbilt University Medical Center, Nashville, Tennessee, Tennessee Valley Healthcare System, Nashville, Tennessee, and Vanderbilt University, Nashville, Tennessee*

Sean K. Wang − *Vanderbilt University, Nashville, Tennessee*

Kathleen Moyer − *Vanderbilt University, Nashville, Tennessee*

Sean K. Bedingfield − *Vanderbilt University, Nashville, Tennessee*

Alyssa R. Merkel − *Vanderbilt University Medical Center, Nashville, Tennessee, and Tennessee Valley Healthcare System, Nashville, Tennessee*

Richard d'Arcy − *Vanderbilt University, Nashville, Tennessee*

Scott A. Guelcher − *Vanderbilt University, Nashville, Tennessee, Vanderbilt University Medical Center, Nashville, Tennessee, and Vanderbilt University, Nashville, Tennessee;* orcid.org/0000-0002-9871-8058

Julie A. Rhoades − *Vanderbilt University Medical Center, Nashville, Tennessee, Tennessee Valley Healthcare System, Nashville, Tennessee, Vanderbilt University, Nashville, Tennessee, and Vanderbilt University Medical Center, Nashville, Tennessee*

Complete contact information is available at: https://pubs.acs.org/10.1021/acsnano.9b04571

Notes

The authors declare no competing financial interest.

ACKNOWLEDGMENTS

This work was supported by NIH Grant No. R01CA163499 (S.A.G. and J.A.S.), VA Merit Award 1I01BX001957 (J.A.S.), and the DOD CDMRP awards W81XWH-15-1-0627 (C.L.D.) and W81XWH-15-1-0622 (J.A.S.).

REFERENCES

(1) Roodman, G. D. Mechanisms of Bone Metastasis. *N. Engl. J. Med.* **2004**, *350*, 1655−1664.

(2) Onishi, T.; Hayashi, N.; Theriault, R. L.; Hortobagyi, G. N.; Ueno, N. T. Future Directions of Bone-Targeted Therapy for Metastatic Breast Cancer. *Nat. Rev. Clin. Oncol.* **2010**, *7*, 641−651.

(3) Baron, R.; Ferrari, S.; Russell, R. G. G. Denosumab and Bisphosphonates: Different Mechanisms of Action and Effects. *Bone* **2011**, *48*, 677−692.

(4) Pozzi, S.; Vallet, S.; Mukherjee, S.; Cirstea, D.; Vaghela, N.; Santo, L.; Rosen, E.; Ikeda, H.; Okawa, Y.; Kiziltepe, T.; Schoonmaker, J.; Xie, W.; Hideshima, T.; Weller, E.; Bouxsein, M. L.; Munshi, N. C.; Anderson, K. C.; Raje, N. High-Dose Zoledronic Acid Impacts Bone Remodeling with Effects on Osteoblastic Lineage and Bone Mechanical Properties. *Clin. Cancer Res.* **2009**, *15*, 5829−5839.

(5) Gnant, M.; Pfeiler, G.; Dubsky, P. C.; Hubalek, M.; Greil, R.; Jakesz, R.; Wette, V.; Balic, M.; Haslbauer, F.; Melbinger, E.; Bjelic-Radisic, V.; Artner-Matuschek, S.; Fitzal, F.; Marth, C.; Sevelda, P.; Mlineritsch, B.; Steger, G. G.; Manfreda, D.; Exner, R.; et al. Adjuvant Denosumab in Breast Cancer (ABCSG-18): A Multicentre, Randomised, Double-Blind, Placebo-Controlled Trial. *Lancet* **2015**, *386*, 433−443.

(6) Lauth, M.; Bergström, A.; Shimokawa, T.; Toftgård, R. Inhibition of GLI-Mediated Transcription and Tumor Cell Growth by Small-Molecule Antagonists. *Proc. Natl. Acad. Sci. U. S. A.* **2007**, *104*, 8455−8460.

(7) Cannonier, S. A.; Gonzales, C. B.; Ely, K.; Guelcher, S. A.; Sterling, J. A. Hedgehog and TGFβ Signaling Converge on Gli2 to Control Bony Invasion and Bone Destruction in Oral Squamous Cell Carcinoma. *Oncotarget* **2016**, *7*, 76062−76075.

(8) Mundy, G. R. Mechanisms of Bone Metastasis. *Cancer* **1997**, *80*, 1546−1556.

(9) Yin, J. J.; Selander, K.; Chirgwin, J. M.; Dallas, M.; Grubbs, B. G.; Wieser, R.; Massagué, J.; Mundy, G. R.; Guise, T. A. TGF-β Signaling Blockade Inhibits PTHrP Secretion by Breast Cancer Cells and Bone Metastases Development. *J. Clin. Invest.* **1999**, *103*, 197−206.

(10) Briscoe, J.; Therond, P. P. The Mechanisms of Hedgehog Signalling and Its Roles in Development and Disease. *Nat. Rev. Mol. Cell Biol.* **2013**, *14*, 416−429.

(11) di Magliano, M. P.; Hebrok, M. Hedgehog Signalling in Cancer Formation and Maintenance. *Nat. Rev. Cancer* **2003**, *3*, 903−911.

(12) Swami, A.; Reagan, M. R.; Basto, P.; Mishima, Y.; Kamaly, N.; Glavey, S.; Zhang, S.; Moschetta, M.; Seevaratnam, D.; Zhang, Y.; Liu, J.; Memarzadeh, M.; Wu, J.; Manier, S.; Shi, J.; Bertrand, N.; Lu, Z. N.; Nagano, K.; Baron, R.; et al. Engineered Nanomedicine for Myeloma and Bone Microenvironment Targeting. *Proc. Natl. Acad. Sci. U. S. A.* **2014**, *111*, 10287−10292.

(13) Cole, L. E.; Vargo-Gogola, T.; Roeder, R. K. Targeted Delivery to Bone and Mineral Deposits Using Bisphosphonate Ligands. *Adv. Drug Delivery Rev.* **2016**, *99*, 12−27.
(14) Qiao, H.; Cui, Z.; Yang, S.; Ji, D.; Wang, Y.; Yang, Y.; Han, X.; Fan, Q.; Qin, A.; Wang, T.; He, X. P.; Bu, W.; Tang, T. Targeting Osteocytes to Attenuate Early Breast Cancer Bone Metastasis by Theranostic Upconversion Nanoparticles with Responsive Plumbagin Release. *ACS Nano* **2017**, *11*, 7259−7273.
(15) Liu, P.; Sun, L.; Zhou, D.; Zhang, P.; Wang, Y.; Li, D.; Li, Q.; Feng, R. J. Development of Alendronate-Conjugated Poly (Lactic-*Co*-Glycolic Acid)-Dextran Nanoparticles for Active Targeting of Cisplatin in Osteosarcoma. *Sci. Rep.* **2015**, *5*, 17387.
(16) Uludag, H.; Yang, J. Targeting Systemically Administered Proteins to Bone by Bisphosphonate Conjugation. *Biotechnol. Prog.* **2002**, *18*, 604−611.
(17) Gittens, S. A.; Bagnall, K.; Matyas, J. R.; Löbenberg, R.; Uludağ, H. Imparting Bone Mineral Affinity to Osteogenic Proteins through Heparin-Bisphosphonate Conjugates. *J. Controlled Release* **2004**, *98*, 255−268.
(18) Bansal, G.; Wright, J. E. I.; Zhang, S.; Zernicke, R. F.; Uludag, H. Imparting Mineral Affinity to Proteins with Thiol-Labile Disulfide Linkages. *J. Biomed. Mater. Res., Part A* **2005**, *74*, 618−628.
(19) Wright, J. E. I.; Gittens, S. A.; Bansal, G.; Kitov, P. I.; Sindrey, D.; Kucharski, C.; Uludağ, H. A Comparison of Mineral Affinity of Bisphosphonate-Protein Conjugates Constructed with Disulfide and Thioether Linkages. *Biomaterials* **2006**, *27*, 769−784.
(20) Murphy, M. B.; Hartgerink, J. D.; Goepferich, A.; Mikos, A. G. Synthesis and *In Vitro* Hydroxyapatite Binding of Peptides Conjugated to Calcium-Binding Moieties. *Biomacromolecules* **2007**, *8*, 2237−2243.
(21) Yamashita, S.; Katsumi, H.; Hibino, N.; Isobe, Y.; Yagi, Y.; Tanaka, Y.; Yamada, S.; Naito, C.; Yamamoto, A. Development of PEGylated Aspartic Acid-Modified Liposome As a Bone-Targeting Carrier for the Delivery of Paclitaxel and Treatment of Bone Metastasis. *Biomaterials* **2018**, *154*, 74−85.
(22) Wang, D.; Miller, S. C.; Shlyakhtenko, L. S.; Portillo, A. M.; Liu, X. M.; Papangkorn, K.; Kopečková, P.; Lyubchenko, Y.; Higuchi, W. I.; Kopeček, J. Osteotropic Peptide That Differentiates Functional Domains of the Skeleton. *Bioconjugate Chem.* **2007**, *18*, 1375−1378.
(23) Chen, F.; Jia, Z.; Rice, K. C.; Reinhardt, R. A.; Bayles, K. W.; Wang, D. The Development of Dentotropic Micelles with Biodegradable Tooth-Binding Moieties. *Pharm. Res.* **2013**, *30*, 2808−2817.
(24) Yamashita, S.; Katsumi, H.; Hibino, N.; Isobe, Y.; Yagi, Y.; Kusamori, K.; Sakane, T.; Yamamoto, A. Development of PEGylated Carboxylic Acid-Modified Polyamidoamine Dendrimers As Bone-Targeting Carriers for the Treatment of Bone Diseases. *J. Controlled Release* **2017**, *262*, 10−17.
(25) Zhou, Z.; Fan, T.; Yan, Y.; Zhang, S.; Zhou, Y.; Deng, H.; Cai, X.; Xiao, J.; Song, D.; Zhang, Q.; Cheng, Y. One Stone with Two Birds: Phytic Acid-Capped Platinum Nanoparticles for Targeted Combination Therapy of Bone Tumors. *Biomaterials* **2019**, *194*, 130−138.
(26) He, C.; Hu, Y.; Yin, L.; Tang, C.; Yin, C. Effects of Particle Size and Surface Charge on Cellular Uptake and Biodistribution of Polymeric Nanoparticles. *Biomaterials* **2010**, *31*, 3657−3666.
(27) Xiao, K.; Li, Y.; Luo, J.; Lee, J. S.; Xiao, W.; Gonik, A. M.; Agarwal, R. G.; Lam, K. S. The Effect of Surface Charge on *In Vivo* Biodistribution of PEG-Oligocholic Acid Based Micellar Nanoparticles. *Biomaterials* **2011**, *32*, 3435−3446.
(28) Gupta, M. K.; Meyer, T. A.; Nelson, C. E.; Duvall, C. L. Poly(PS-*b*-DMA) Micelles for Reactive Oxygen Species Triggered Drug Release. *J. Controlled Release* **2012**, *162*, 591−598.
(29) Gupta, M. K.; Martin, J. R.; Werfel, T. A.; Shen, T.; Page, J. M.; Duvall, C. L. Cell Protective, ABC Triblock Polymer-Based Thermoresponsive Hydrogels with ROS-Triggered Degradation and Drug Release. *J. Am. Chem. Soc.* **2014**, *136*, 14896−14902.
(30) Poole, K. M.; Nelson, C. E.; Joshi, R. V.; Martin, J. R.; Gupta, M. K.; Haws, S. C.; Kavanaugh, T. E.; Skala, M. C.; Duvall, C. L. ROS-Responsive Microspheres for on Demand Antioxidant Therapy in a Model of Diabetic Peripheral Arterial Disease. *Biomaterials* **2015**, *41*, 166−175.
(31) Gupta, M. K.; Martin, J. R.; Dollinger, B. R.; Hattaway, M. E.; Duvall, C. L. Thermogelling, ABC Triblock Copolymer Platform for Resorbable Hydrogels with Tunable, Degradation-Mediated Drug Release. *Adv. Funct. Mater.* **2017**, *27*, 1704107.
(32) Ross, R. D.; Roeder, R. K. Binding Affinity of Surface Functionalized Gold Nanoparticles to Hydroxyapatite. *J. Biomed. Mater. Res., Part A* **2011**, *99A*, 58−66.
(33) Ross, R. D.; Cole, L. E.; Roeder, R. K. Relative Binding Affinity of Carboxylate-, Phosphonate-, and Bisphosphonate-Functionalized Gold Nanoparticles Targeted to Damaged Bone Tissue. *J. Nanopart. Res.* **2012**, *14*, 1175.
(34) Li, C.; Zhang, Y.; Chen, G.; Hu, F.; Zhao, K.; Wang, Q. Engineered Multifunctional Nanomedicine for Simultaneous Stereotactic Chemotherapy and Inhibited Osteolysis in an Orthotopic Model of Bone Metastasis. *Adv. Mater.* **2017**, *29*, 1605754.
(35) Uddin, M. J.; Werfel, T. A.; Crews, B. C.; Gupta, M. K.; Kavanaugh, T. E.; Kingsley, P. J.; Boyd, K.; Marnett, L. J.; Duvall, C. L. Fluorocoxib A Loaded Nanoparticles Enable Targeted Visualization of Cyclooxygenase-2 in Inflammation and Cancer. *Biomaterials* **2016**, *92*, 71−80.
(36) Wang, L.; Kilcher, G.; Tirelli, N. Synthesis and Properties of Amphiphilic Star Polysulfides. *Macromol. Biosci.* **2007**, *7*, 987−998.
(37) Du, F.; Liu, Y. G.; Scott, E. A. Immunotheranostic Polymersomes Modularly Assembled from Tetrablock and Diblock Copolymers with Oxidation-Responsive Fluorescence. *Cell. Mol. Bioeng.* **2017**, *10*, 357−370.
(38) Costa, A.; Scholer-Dahirel, A.; Mechta-Grigoriou, F. The Role of Reactive Oxygen Species and Metabolism on Cancer Cells and Their Microenvironment. *Semin. Cancer Biol.* **2014**, *25*, 23−32.
(39) Szatrowski, T. P.; Nathan, C. F. Production of Large Amounts of Hydrogen Peroxide by Human Tumor Cells. *Cancer Res.* **1991**, *51*, 794−798.
(40) Napoli, A.; Valentini, M.; Tirelli, N.; Muller, M.; Hubbell, J. A. Oxidation-Responsive Polymeric Vesicles. *Nat. Mater.* **2004**, *3*, 183−189.
(41) Šprincl, L.; Vacík, J.; Kopeček, J.; Lím, D. Biological Tolerance of Poly(N-Substituted Methacrylamides). *J. Biomed. Mater. Res.* **1971**, *5*, 197−205.
(42) Ulbrich, W.; Lamprecht, A. Fluorimetric Quantification of Clodronate and Alendronate in Aqueous Samples and in Serum. *Talanta* **2011**, *84*, 437−442.
(43) Corns, C. M.; Ludman, C. J. Some Observations on the Nature of the Calcium-Cresolphthalein Complexone Reaction and Its Relevance to the Clinical Laboratory. *Ann. Clin. Biochem.* **1987**, *24*, 345−351.
(44) Elmalla, S. F.; Mansour, F. R. A Simple Innovative Spectrofluorometric Method for the Determination of Alendronate in Bulk and in Pharmaceutical Tablets. *Luminescence* **2019**, *34*, 375−381.
(45) Liedtke, R. J.; Kroon, G.; Batjer, J. D. Centrifugal Analysis with Automated Sequential Reagent Addition: Measurement of Serum Calcium. *Clin. Chem.* **1981**, *27*, 2025−2028.
(46) Low, S. A.; Kopeček, J. Targeting Polymer Therapeutics to Bone. *Adv. Drug Delivery Rev.* **2012**, *64*, 1189−1204.
(47) Leu, C. T.; Luegmayr, E.; Freedman, L. P.; Rodan, G. A.; Reszka, A. A. Relative Binding Affinities of Bisphosphonates for Human Bone and Relationship to Antiresorptive Efficacy. *Bone* **2006**, *38*, 628−636.
(48) Wang, J.; Wu, W.; Zhang, Y.; Wang, X.; Qian, H.; Liu, B.; Jiang, X. The Combined Effects of Size and Surface Chemistry on the Accumulation of Boronic Acid-Rich Protein Nanoparticles in Tumors. *Biomaterials* **2014**, *35*, 866−878.
(49) Valencia, P. M.; Pridgen, E. M.; Rhee, M.; Langer, R.; Farokhzad, O. C.; Karnik, R. Microfluidic Platform for Combinatorial Synthesis and Optimization of Targeted Nanoparticles for Cancer Therapy. *ACS Nano* **2013**, *7*, 10671−10680.
(50) Werfel, T. A.; Jackson, M. A.; Kavanaugh, T. E.; Kirkbride, K. C.; Miteva, M.; Giorgio, T. D.; Duvall, C. Combinatorial Optimization of PEG Architecture and Hydrophobic Content Improves Ternary SiRNA Polyplex Stability, Pharmacokinetics, and Potency *In Vivo*. *J. Controlled Release* **2017**, *255*, 12−26.

https://dx.doi.org/10.1021/acsnano.9b04571
ACS Nano 2020, 14, 311−327

(51) Lu, Y.; Zhang, E.; Yang, J.; Cao, Z. Strategies to Improve Micelle Stability for Drug Delivery. *Nano Res.* **2018**, *11*, 4985−4998.
(52) Kim, S.; Shi, Y.; Kim, J. Y.; Park, K.; Cheng, J.-X. Overcoming the Barriers in Micellar Drug Delivery: Loading Efficiency, *In Vivo* Stability, and Micelle−Cell Interaction. *Expert Opin. Drug Delivery* **2010**, *7*, 49−62.
(53) Bertrand, N.; Leroux, J. C. The Journey of a Drug-Carrier in the Body: An Anatomo-Physiological Perspective. *J. Controlled Release* **2012**, *161*, 152−163.
(54) Perry, J. L.; Reuter, K. G.; Kai, M. P.; Herlihy, K. P.; Jones, S. W.; Luft, J. C.; Napier, M.; Bear, J. E.; Desimone, J. M. PEGylated PRINT Nanoparticles: The Impact of PEG Density on Protein Binding, Macrophage Association, Biodistribution, and Pharmacokinetics. *Nano Lett.* **2012**, *12*, 5304−5310.
(55) Yamamoto, Y.; Nagasaki, Y.; Kato, Y.; Sugiyama, Y.; Kataoka, K. Long-Circulating Poly(Ethylene Glycol)-Poly(D,L-Lactide) Block Copolymer Micelles with Modulated Surface Charge. *J. Controlled Release* **2001**, *77*, 27−38.
(56) Kamaly, N.; Xiao, Z.; Valencia, P. M.; Radovic-Moreno, A. F.; Farokhzad, O. C. Targeted Polymeric Therapeutic Nanoparticles: Design, Development and Clinical Translation. *Chem. Soc. Rev.* **2012**, *41*, 2971−3010.
(57) Clark, A. J.; Wiley, D. T.; Zuckerman, J. E.; Webster, P.; Chao, J.; Lin, J.; Yen, Y.; Davis, M. E. CRLX101 Nanoparticles Localize in Human Tumors and Not in Adjacent, Nonneoplastic Tissue after Intravenous Dosing. *Proc. Natl. Acad. Sci. U. S. A.* **2016**, *113*, 3850−3854.
(58) Zhao, Y.-p.; Ye, W.-l.; Liu, D.-z.; Cui, H.; Cheng, Y.; Liu, M.; Zhang, B.-l.; Mei, Q.-b.; Zhou, S.-y. Redox and pH Dual Sensitive Bone Targeting Nanoparticles to Treat Breast Cancer Bone Metastases and Inhibit Bone Resorption. *Nanoscale* **2017**, *9*, 6264−6277.
(59) Sterling, J. A.; Oyajobi, B. O.; Grubbs, B.; Padalecki, S. S.; Munoz, S. A.; Gupta, A.; Story, B.; Zhao, M.; Mundy, G. R. The Hedgehog Signaling Molecule Gli2 Induces Parathyroid Hormone-Related Peptide Expression and Osteolysis in Metastatic Human Breast Cancer Cells. *Cancer Res.* **2006**, *66*, 7548−7553.
(60) Johnson, R. W.; Nguyen, M. P.; Padalecki, S. S.; Grubbs, B. G.; Merkel, A. R.; Oyajobi, B. O.; Matrisian, L. M.; Mundy, G. R.; Sterling, J. A. TGF-Beta Promotion of Gli2-Induced Expression of Parathyroid Hormone-Related Protein, an Important Osteolytic Factor in Bone Metastasis, Is Independent of Canonical Hedgehog Signaling. *Cancer Res.* **2011**, *71*, 822−831.
(61) Thiyagarajan, S.; Bhatia, N.; Reagan-Shaw, S.; Cozma, D.; Thomas-Tikhonenko, A.; Ahmad, N.; Spiegelman, V. S. Role of GLI2 Transcription Factor in Growth and Tumorigenicity of Prostate Cells. *Cancer Res.* **2007**, *67*, 10642−10646.
(62) Ruppender, N. S.; Merkel, A. R.; Martin, T. J.; Mundy, G. R.; Sterling, J. A.; Guelcher, S. A. Matrix Rigidity Induces Osteolytic Gene Expression of Metastatic Breast Cancer Cells. *PLoS One* **2010**, *5*, e15451.
(63) Page, J. M.; Merkel, A. R.; Ruppender, N. S.; Guo, R.; Dadwal, U. C.; Cannonier, S. A.; Basu, S.; Guelcher, S. A.; Sterling, J. A. Matrix Rigidity Regulates the Transition of Tumor Cells to a Bone-Destructive Phenotype through Integrin B3 and TGF-β Receptor Type II. *Biomaterials* **2015**, *64*, 33−44.
(64) Discher, D. E. Tissue Cells Feel and Respond to the Stiffness of Their Substrate. *Science* **2005**, *310*, 1139−1143.
(65) Allen, S. D.; Liu, Y. G.; Bobbala, S.; Cai, L.; Hecker, P. I.; Temel, R.; Scott, E. A. Polymersomes Scalably Fabricated *via* Flash Nanoprecipitation Are Non-Toxic in Non-Human Primates and Associate with Leukocytes in the Spleen and Kidney Following Intravenous Administration. *Nano Res.* **2018**, *11*, 5689−5703.
(66) Bamias, A.; Kastritis, E.; Bamia, C.; Moulopoulos, L. A.; Melakopoulos, I.; Bozas, G.; Koutsoukou, V.; Gika, D.; Anagnostopoulos, A.; Papadimitriou, C.; Terpos, E.; Dimopoulos, M. A. Osteonecrosis of the Jaw in Cancer after Treatment with Bisphosphonates: Incidence and Risk Factors. *J. Clin. Oncol.* **2005**, *23*, 8580−8587.
(67) Coleman, R.; Woodward, E.; Brown, J.; Cameron, D.; Bell, R.; Dodwell, D.; Keane, M.; Gil, M.; Davies, C.; Burkinshaw, R.; Houston, S. J.; Grieve, R. J.; Barrett-Lee, P. J.; Thorpe, H. Safety of Zoledronic Acid and Incidence of Osteonecrosis of the Jaw (ONJ) during Adjuvant Therapy in a Randomised Phase III Trial (AZURE: BIG 01−04) for Women with Stage II/III Breast Cancer. *Breast Cancer Res. Treat.* **2011**, *127*, 429−438.
(68) Smith, M. R.; Saad, F.; Coleman, R.; Shore, N.; Fizazi, K.; Tombal, B.; Miller, K.; Sieber, P.; Karsh, L.; Damião, R.; Tammela, T. L.; Egerdie, B.; Van Poppel, H.; Chin, J.; Morote, J.; Gómez-Veiga, F.; Borkowski, T.; Ye, Z.; Kupic, A.; et al. Denosumab and Bone-Metastasis-Free Survival in Men with Castration-Resistant Prostate Cancer: Results of a Phase 3, Randomised, Placebo-Controlled Trial. *Lancet* **2012**, *379*, 39−46.
(69) Yang, S. P.; Kim, T. W. B.; Boland, P. J.; Farooki, A. Retrospective Review of Atypical Femoral Fracture in Metastatic Bone Disease Patients Receiving Denosumab Therapy. *Oncologist* **2017**, *22*, 438−444.
(70) Carbone, E. J.; Rajpura, K.; Allen, B. N.; Cheng, E.; Ulery, B. D.; Lo, K. W. H. Osteotropic Nanoscale Drug Delivery Systems Based on Small Molecule Bone-Targeting Moieties. *Nanomedicine* **2017**, *13*, 37−47.
(71) Sinder, B. P.; Zweifler, L.; Koh, A. J.; Michalski, M. N.; Hofbauer, L. C.; Aguirre, J. I.; Roca, H.; McCauley, L. K. Bone Mass Is Compromised by the Chemotherapeutic Trabectedin in Association With Effects on Osteoblasts and Macrophage Efferocytosis. *J. Bone Miner. Res.* **2017**, *32*, 2116−2127.
(72) Fan, C.; Georgiou, K. R.; Morris, H. A.; McKinnon, R. A.; Keefe, D. M. K.; Howe, P. R.; Xian, C. J. Combination Breast Cancer Chemotherapy with Doxorubicin and Cyclophosphamide Damages Bone and Bone Marrow in a Female Rat Model. *Breast Cancer Res. Treat.* **2017**, *165*, 41−51.
(73) Guise, T. A.; Yin, J. J.; Taylor, S. D.; Kumagai, Y.; Dallas, M.; Boyce, B. F.; Yoneda, T.; Mundy, G. R. Evidence for a Causal Role of Parathyroid Hormone-Related Protein in the Pathogenesis of Human Breast Cancer-Mediated Osteolysis. *J. Clin. Invest.* **1996**, *98*, 1544−1549.
(74) Saito, H.; Tsunenari, T.; Onuma, E.; Sato, K.; Ogata, E.; Yamada-Okabe, H. Humanized Monoclonal Antibody against Parathyroid Hormone-Related Protein Suppresses Osteolytic Bone Metastasis of Human Breast Cancer Cells Derived from MDA-MB-231. *Anticancer Res.* **2005**, *25*, 3817−3823.
(75) He, Y.; Zhu, T.; Liu, L.; Shi, X.; Lin, Z. Modifying Collagen with Alendronate Sodium for Bone Regeneration Applications. *RSC Adv.* **2018**, *8*, 16762−16772.
(76) Jackson, M. A.; Werfel, T. A.; Curvino, E. J.; Yu, F.; Kavanaugh, T. E.; Sarett, S. M.; Dockery, M. D.; Kilchrist, K. V.; Jackson, A. N.; Giorgio, T. D.; Duvall, C. L. Zwitterionic Nanocarrier Surface Chemistry Improves SiRNA Tumor Delivery and Silencing Activity Relative to Polyethylene Glycol. *ACS Nano* **2017**, *11*, 5680−5696.
(77) Hengst, V.; Oussoren, C.; Kissel, T.; Storm, G. Bone Targeting Potential of Bisphosphonate-Targeted Liposomes: Preparation, Characterization and Hydroxyapatite Binding *In Vitro*. *Int. J. Pharm.* **2007**, *331*, 224−227.
(78) Wang, H.; Liu, J.; Tao, S.; Chai, G.; Wang, J.; Hu, F.-Q.; Yuan, H. Tetracycline-Grafted PLGA Nanoparticles As Bone-Targeting Drug Delivery System. *Int. J. Nanomed.* **2015**, *10*, 5671−5685.
(79) Guo, R.; Lu, S.; Merkel, A. R.; Sterling, J. A.; Guelcher, S. A. Substrate Modulus Regulates Osteogenic Differentiation of Rat Mesenchymal Stem Cells through Integrin B1 and BMP Receptor Type IA. *J. Mater. Chem. B* **2016**, *4*, 3584−3593.
(80) Mbalaviele, G.; Chen, H.; Boyce, B. F.; Mundy, G. R.; Yoneda, T. The Role of Cadherin in the Generation of Multinucleated Osteoclasts from Mononuclear Precursors in Murine Marrow. *J. Clin. Invest.* **1995**, *95*, 2757−2765.
(81) Michigami, T.; Shimizu, N.; Williams, P. J.; Niewolna, M.; Dallas, S. L.; Mundy, G. R.; Yoneda, T. Cell-Cell Contact between Marrow Stromal Cells and Myeloma Cells *via* VCAM-1 and Alpha(4)Beta(1)-

https://dx.doi.org/10.1021/acsnano.9b04571
ACS Nano 2020, 14, 311−327

Integrin Enhances Production of Osteoclast-Stimulating Activity. *Blood* **2000**, *96*, 1953−1960.
(82) Wright, L. E.; Ottewell, P. D.; Rucci, N.; Peyruchaud, O.; Pagnotti, G. M.; Chiechi, A.; Buijs, J. T.; Sterling, J. A. Murine Models of Breast Cancer Bone Metastasis. *BoneKEy Rep.* **2016**, *5*, 804.
(83) Lam, M. H.; Thomas, R. J.; Loveland, K. L.; Schilders, S.; Gu, M.; Martin, T. J.; Gillespie, M. T.; Jans, D. A. Nuclear Transport of Parathyroid Hormone (PTH)-Related Protein Is Dependent on Microtubules. *Mol. Endocrinol.* **2002**, *16*, 390−401.
(84) Ansari, N.; Ho, P. W.; Crimeen-Irwin, B.; Poulton, I. J.; Brunt, A. R.; Forwood, M. R.; Divieti Pajevic, P.; Gooi, J. H.; Martin, T. J.; Sims, N. A. Autocrine and Paracrine Regulation of the Murine Skeleton by Osteocyte-Derived Parathyroid Hormone-Related Protein. *J. Bone Miner. Res.* **2018**, *33*, 137−153.

https://dx.doi.org/10.1021/acsnano.9b04571
ACS Nano 2020, 14, 311−327